ACS NANO

www.acsnano.org

Article

Extending Polarization Detection to the Infrared Region via Sb_2Se_3 Nanowires/PbS Quantum Dots Heterojunctions

Kai Zhang,[#] Wenhao Ran,[#] Yali Yu,[#] Pan Wang, Huichen Cao, Bin Dai, Yechao Han, Linjuan Guo, Zhiqiang Li, Juehan Yang, Hui Guo, Lihong Bao, Guozhen Shen,* Zhongming Wei,* Haitao Yang,* and Hongjun Gao

Cite This: *ACS Nano* 2026, 20, 2774−2788

Read Online

ACCESS | Metrics & More | Article Recommendations | Supporting Information

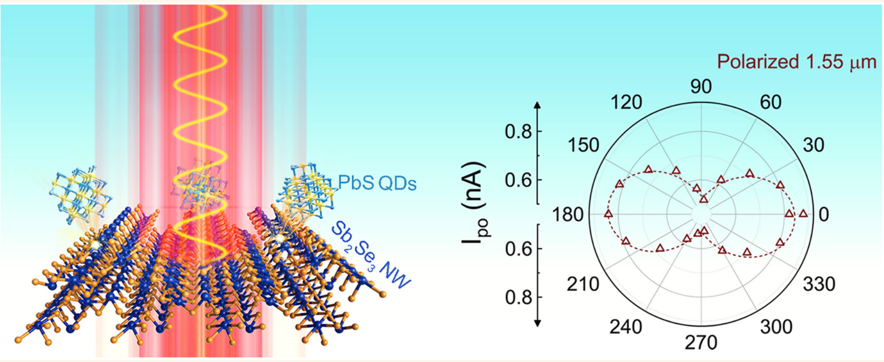

ABSTRACT: Polarization-sensitive infrared photodetectors find broad use in military and industrial fields and thus have emerged as a research hotspot in recent years. Owing to the intrinsic asymmetric structure, Sb_2Se_3 nanowires hold significant application in polarization detection. However, constrained by bandgap width, their polarization detection wavelength is limited to below 1000 nm. In this work, Sb_2Se_3 nanowires (NWs)/PbS quantum dots (QDs) heterojunctions were fabricated, with the carrier transport efficiency at the heterojunction interface enhanced via long-to-short-chain ligand exchange. Compared with pure Sb_2Se_3 NW-based photodetectors (PDs), the Sb_2Se_3 NWs/PbS QDs heterojunction-based counterparts not only have their detection wavelength extended to 1.55 μm but, more notably, their polarization detection wavelength is also extended to 1.55 μm. The photodetector exhibits responsivities (R_λ) of 1.12 A/W and 0.86 A/W for 1.31 and 1.55 μm incident lasers, with measured dichroic ratios of 1.38 and 1.58, respectively, for the polarized light at these two wavelengths. The ultraviolet photoelectron spectroscopy (UPS) analysis reveals that the separation of photogenerated carriers at the heterojunction interface enhances the absorption of infrared polarized light by the defect energy levels in Sb_2Se_3 NWs, thereby extending the polarized photoresponse wavelength of the heterojunction to 1.55 μm. Moreover, by employing convolution kernels constructed from the infrared polarization R_λ of the Sb_2Se_3/PbS heterojunction-based PD, the artificial neural network (ANN) can effectively extract feature information, reduce redundant data and noise, and facilitate image recognition. These outstanding polarization detection performances demonstrate that extending the polarization detection wavelength to the infrared region via QDs coupling is an innovative and reliable approach with promising prospects for further applications.

KEYWORDS: *Sb_2Se_3 nanowires, PbS quantum dots, heterojunction, photodetector, polarization detection, image recognition*

The polarized infrared imaging holds great significance for advancing astronomy, biological diagnosis, military, and industrial applications; thus, polarization-sensitive infrared photodetectors have recently emerged as a new research hotspot and are widely adopted.[1−8] Currently, researches on polarization detectors primarily focus on semiconductor materials with low-symmetry structures—such as those belonging to the orthorhombic, monoclinic, and trigonal systems—with examples including Sb_2S_3, ReS_2, Sb_2Se_3, GeSe, SnSe, SiP_2, and β-Ga_2O_3, among others.[9−17] In these materials, the energy band dispersion in momentum space varies significantly along different high-symmetry directions, leading to anisotropic responses in both physical properties and device performance as a function of the in-plane angle.[10,15] For infrared polarization detection, low-symmetry semiconductors

Received: September 26, 2025
Revised: January 4, 2026
Accepted: January 5, 2026
Published: January 12, 2026

ACS Publications

https://doi.org/10.1021/acsnano.5c16680

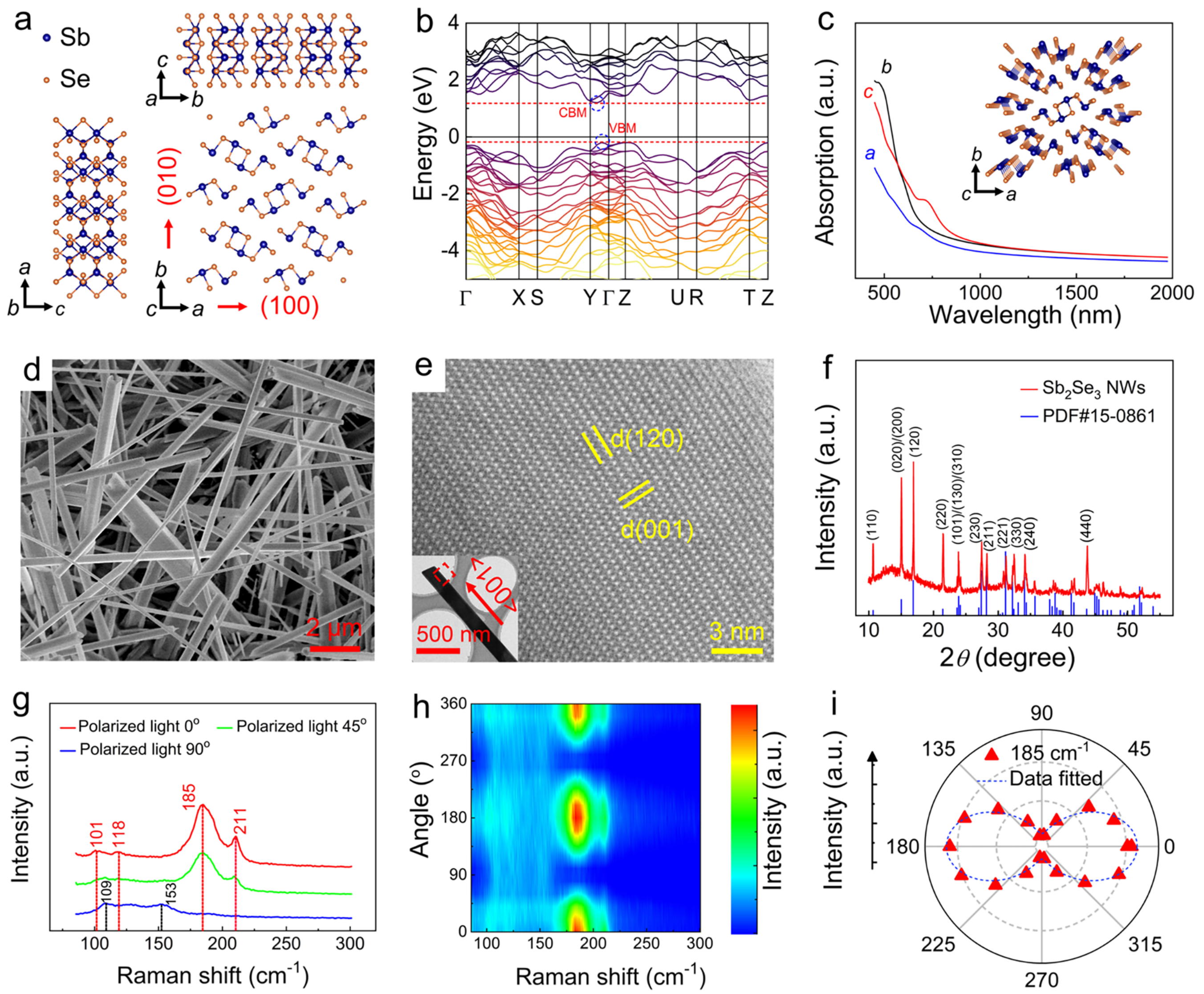

Figure 1. DFT calculation and experimental characterization of the Sb_2Se_3 NWs. (a) Crystal structure of the Sb_2Se_3 observed on three different crystal planes. (b) Calculated band structure of the Sb_2Se_3. (c) Calculated optical absorption coefficient along *a*-axis, *b*-axis and *c*-axis. (d) SEM image of as-grown Sb_2Se_3 NWs. (e, f) HRTEM and XRD results of the Sb_2Se_3 NWs. (g) Raman spectra of the Sb_2Se_3 NW measured with a polarized 532 nm laser at 0 °, 45 ° and 90 °. (h) 2D mapping image of the Sb_2Se_3 NW Raman spectra corresponding to the polarization angle (*θ*) of the incident laser. (i) Polar plots depicting the Raman intensity of the 184 cm^{-1} peak with respect to *θ*.

with narrow bandgaps are required; primary examples include black phosphorus (BP), b-AsP, Te, and $ZrTe_3$, to name a few.[7,18−20] However, the pool of such low-symmetry narrow-bandgap semiconductors remains relatively limited, which poses the development of novel structural systems for the infrared polarization detection as an entirely new challenge. Heterojunction construction is a widely used strategy in general photodetectors. Through band engineering, a well-designed heterojunction structure can effectively facilitate the separation of photogenerated carriers at the interface, enhance photoresponse performance, and extend the detection wavelength range.[21,22] For instance, the constructed InGaAs/GeS core−shell type-II heterojunction exhibits a photodetection performance that is 2 orders of magnitude higher than that of pure InGaAs.[23] Recently, heterojunction-based devices utilizing anisotropic materials (e.g., GeAs/InSe, $MoS_2/SnSe_2$, $ReS_2/MoSe_2$, Gr/$PdSe_2$/Ge, Sb_2Se_3/n-GaN, Sb_2Se_3/Si) have been proposed for developing polarization-sensitive photodetectors (PDs).[14,24−28] While these studies have demonstrated improved polarization sensitivity, research focused on extending the polarization detection wavelength to the infrared region via heterojunction effects remains relatively limited and thus merits further investigation.

Antimony selenide nanowires (Sb_2Se_3 NWs) stand out as prototypical semiconductors for applications in photodetection and photovoltaic devices, owing to their large optical absorption coefficient ($>10^5$ cm^{-1} for visible light), suitable bandgap (1.1−1.3 eV), nontoxicity, and earth abundance.[13,29−31] With an orthorhombic crystal structure, Sb_2Se_3 NWs are composed of covalently bonded one-dimensional ribbon-like $(Sb_4Se_6)_n$ units, which are connected via van der Waals forces along the [100] direction (*x*-axis) and [010] direction (*y*-axis).[32−34] Precisely, this one-dimensional geometry and low-symmetry structure endow them with significant in-plane anisotropy in carrier transport and light absorption—properties that make them ideal for fabricating polarization-sensitive PDs. For example, in a study by Zhao et al., Sb_2Se_3 flakes synthesized via sodium-mediated chemical vapor

https://doi.org/10.1021/acsnano.5c16680
ACS Nano 2026, 20, 2774−2788

deposition (CVD) method exhibited a dichroic ratio of 2.5 for 532 nm polarized light. Similarly, Wan et al. reported that polarized PDs based on Sb_2Se_3 microbelts/n-GaN heterojunctions achieved a dichroic ratio of 1.37 for 940 nm polarized light.[27,33] However, due to bandgap constraints, the polarization detection wavelength of Sb_2Se_3-based polarized PDs has thus far been limited to below 1000 nm, regardless of whether they rely on Sb_2Se_3 nanostructures or Sb_2Se_3-based heterojunctions.[13,28,31−34]

Quantum dots (QD) coupling serves as an effective approach to enhancing the performance of photodetectors. Lead sulfide (PbS) QDs are the versatile infrared detection material with a diameter-dependent tunable bandgap (0.6−1.6 eV), and they also possess several key advantages, including a high molar absorption coefficient, well-established solution-phase synthesis techniques, and low fabrication costs.[35−38] Notably, the transport efficiency of photogenerated carriers at the QD interface can be boosted by ligand engineering, which involves replacing the long-chain ligands on QD surfaces with short-chain counterparts.[35−37,39] These characteristics facilitate the widespread integration of PbS QDs into heterojunction devices while enhancing the infrared detection performance of such devices. In the literature, mixed-dimensional heterostructure PDs, including Si NWs/PbS QDs, 2D Bi_2O_2Se/PbS QDs, and IGZO films/PbS QDs, have all been demonstrated to extend their detection wavelength to the infrared region.[39−41] Whether PbS coupling can extend the polarization detection wavelength into the infrared region remains a worthwhile avenue for exploration.

In this work, high-quality Sb_2Se_3 NWs were grown via the chemical vapor deposition (CVD) method, while PbS QDs with highly uniform diameters were synthesized by using a liquid-phase method. PbS QDs were spin-coated onto the surfaces of as-grown Sb_2Se_3 NWs to form Sb_2Se_3 NWs/PbS QDs heterojunctions. Concurrently, ligand engineering was employed to replace the long-chain ligands with short-chain ligands. The PDs were fabricated using Sb_2Se_3 NWs/PbS QDs heterojunctions (simplified as Sb_2Se_3/PbS). Compared with PDs based on pure Sb_2Se_3 NWs, the heterojunction devices exhibit enhanced photoelectric detection performance: not only is their detection wavelength extended to 1.55 μm but, more impressively, their polarization detection wavelength is extended to 1.55 μm as well. For incident lasers at 1.31 and 1.55 μm, the photodetector demonstrates a responsivity (R_λ) of 1.12 and 0.86 A/W, respectively. Corresponding to these two wavelengths, the dichroic ratios measured under polarized light are 1.38 and 1.58. Ultraviolet photoelectron spectroscopy (UPS) measurements were conducted to elucidate the polarization detection wavelength extension mechanism. The separation of photogenerated carriers at the heterojunction interface enhances the absorption of 1.55 μm polarized light by the defect energy levels in Sb_2Se_3 NWs, thereby extending the wavelength of the polarized photoresponse to 1.55 μm. What's more, five convolution kernels are constructed from the infrared polarization R_λ of Sb_2Se_3/PbS-heterojunction PD. The ANN preprocessing by means of these convolution kernels can effectively extract relevant feature information, reduce redundant data and noise, and facilitate the image recognition process. These exceptional infrared polarization detection properties of the Sb_2Se_3/PbS-heterojunction PDs manifest that QDs coupling is an innovative and reliable approach to extend the polarization detection wavelength to the infrared region, a strategy that thus warrants further developments and applications.

RESULTS AND DISCUSSION

Antimony selenide (Sb_2Se_3) is an intrinsically anisotropic material with an orthorhombic crystal structure, where the lattice parameters are a = 11.62 Å, b = 11.77 Å, and c = 3.962 Å.[32,42−44] Figure 1a shows the lattice structures of Sb_2Se_3 in the *ab*-plane, *ca*-plane, and *bc*-plane, which are visualized by using VESTA software. Notably, the covalently linked one-dimensional (1D) ribbon-structured $(Sb_4Se_6)_n$ units are interconnected along the [100] (x-axis) and [010] (y-axis) directions by van der Waals forces. To clarify the energy band structure of Sb_2Se_3 first-principles computations were performed within the framework of density functional theory (DFT) utilizing the Vienna Ab initio Simulation Package (VASP).[45] Core electrons were described using the projector augmented wave (PAW) method, and the exchange-correlation potential was treated using the generalized gradient approximation (GGA) with the Perdew−Burke−Ernzerhof (PBE) functional.[46−48] For more precise calculations of the electronic band structures, the HSE06 (Heyd-Scuseria-Ernzerhof) hybrid functional was employed.[49] The calculated results are presented in Figure 1b, which show that Sb_2Se_3 is a quasi-direct bandgap semiconductor with a bandgap of 1.4 eV. This value is close to both the experimental results we will discuss below and the values reported in the literature.[30,50] The computed optical absorption data are shown in Figure 1c. In the wavelength range from 450 to 570 nm, the optical absorption along the b-axis is greater than that along the c-axis and a-axis. However, starting from 570 up to 1000 nm, the optical absorption along the c-axis is significantly higher than that along other axis. This indicates that in the primary visible-to-near-infrared region, the strongest polarized absorption occurs along the c-axis, implying that Sb_2Se_3 is viable for fabricating visible-near-infrared polarized photodetectors which is well consistent with the previous literature reports.[13,31]

In this work, Sb_2Se_3 NWs were fabricated by CVD method in a horizontal quartz tube furnace. The specific experimental details are described in the Experiment Section. Figure 1d is the SEM image of as-grown Sb_2Se_3 NWs that exhibit a relatively large diameter with a distribution ranging from several hundred nanometers to 2 μm. To gain deeper insight into the microstructure of the as-synthesized Sb_2Se_3 NWs, transmission electron microscopy (TEM) and energy-dispersive X-ray spectroscopy (EDS) were performed. Figures S4 and 1e presents the EDS elemental mapping and TEM image of a representative Sb_2Se_3 NW. From the EDS results, it is evident that Sb and Se elements are uniformly distributed along the NW. The inset of Figure 1e shows that the Sb_2Se_3 NW has an approximate diameter of 250 nm and a smooth surface. High-resolution TEM (HRTEM) characterization was carried out on the red rectangular region, while fast Fourier transform (FFT) analysis was performed independently; the results are presented in Figures 1e and S5, respectively. The clear high-resolution lattice fringes are observed with no obvious crystalline defects. The measured interplanar spacings of 0.39 and 0.52 nm correspond to the (001) and (120) lattice planes of orthorhombic Sb_2Se_3.[32,44] It is obvious that the Sb_2Se_3 NW has an axial growth orientation of ⟨001⟩, which aligns with the direction of strongest light absorption, as supported by our previous theoretical calculations. To further

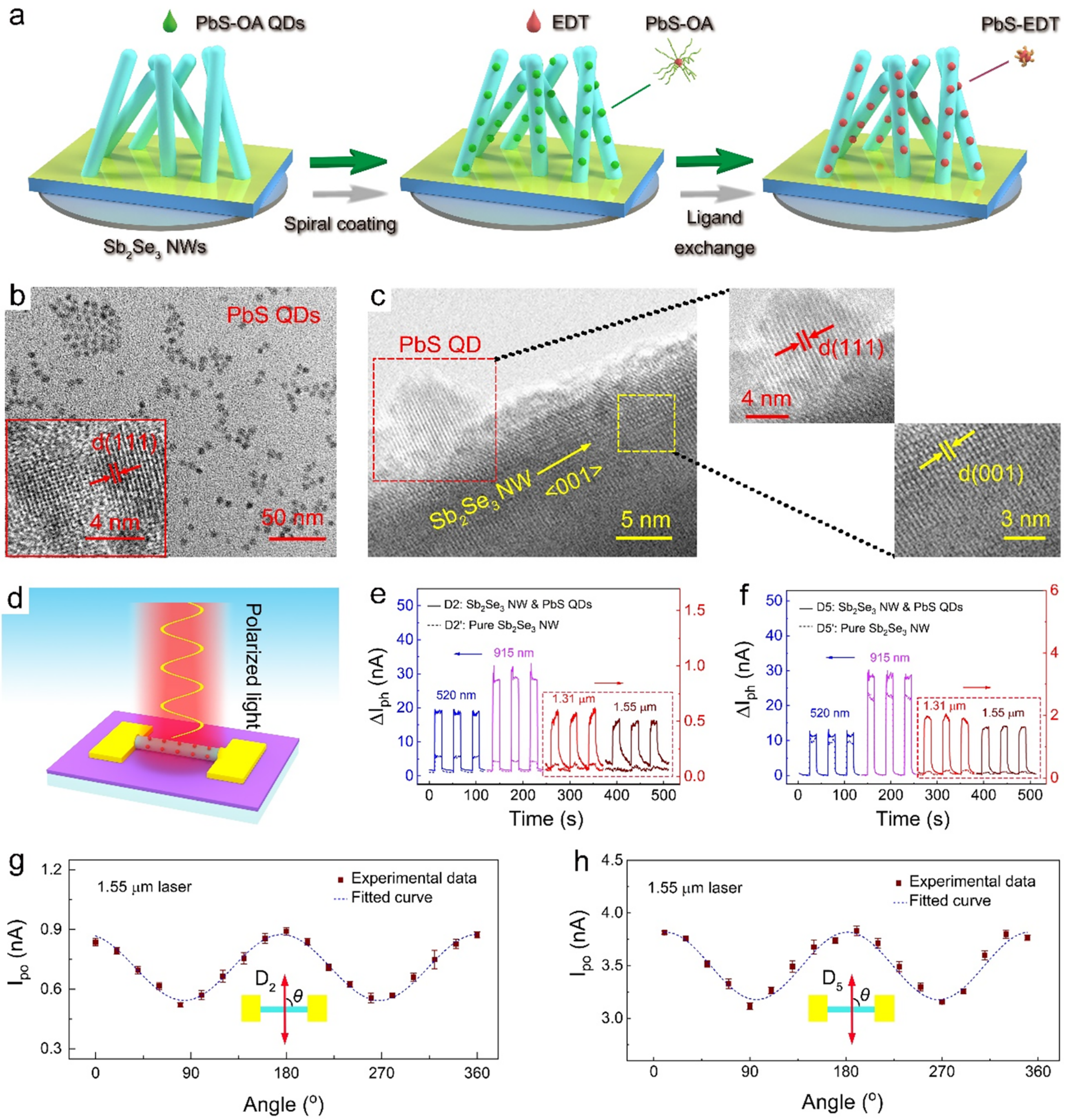

Figure 2. Fabrication of Sb_2Se_3/PbS heterojunction and the photoresponse properties of the heterojunction photodetector. (a) Schematic illustration of Sb_2Se_3/PbS heterojunction fabrication with long-to-short-chain ligand exchange. (b) STEM and HRTEM images of as-synthesized PbS QDs. (c) HRTEM image of a Sb_2Se_3 /PbS heterojunction. (d) Schematic illustration of the Sb_2Se_3/PbS-heterojunction polarization PD. (e) Performance comparison between the Sb_2Se_3/PbS-heterojunction PD (D2) and the pure Sb_2Se_3 NW PD (D2′), and (f) performance comparison of another set of devices (D5 and D5′). (g, h) Polarization angle-dependent photoresponse of device D2 to 1.55 μm incident laser, and device D5 to 1.55 μm incident laser. The inset illustrates the definition of the polarization angle θ for the incident linearly polarized laser.

determine the crystalline structure of the Sb_2Se_3 NWs, X-ray diffraction (XRD) analysis was performed, with the corresponding diffraction pattern shown in Figure 1e. As indicated by the XRD results, all diffraction peaks correspond to orthorhombic Sb_2Se_3 with lattice parameters a = 11.633 Å, b = 11.78 Å, and c = 3.985 Å (PDF#15−0861).[32,42−44] These unit cell parameters are consistent with the modeling used in our previous theoretical calculations. The chemical state of as-grown Sb_2Se_3 NWs was investigated via X-ray photoelectron spectroscopy (XPS), with the results shown in Figure S6. Compared to earlier studies, slight peak shifts are observed, which are attributed to the size effect of the nanowires and will not be elaborated on here.[51,52] After Gaussian/Lorentzian fitting, the Sb 4d spectrum deconvolves into Sb $4d_{5/2}$ at 34.08 eV and Sb $4d_{3/2}$ at 35.33 eV, while the Se 3d spectrum splits into Se $3d_{5/2}$ at 54.90 eV and Se $3d_{3/2}$ at 55.71 eV, a

https://doi.org/10.1021/acsnano.5c16680
ACS Nano 2026, 20, 2774−2788

phenomenon arising from the spin−orbit splitting (s.o.s) effect.[33,53−55] Notably, no additional peaks are detectable in either the Sb 4d or Se 3d spectra, indicating the absence of other antimony- or selenium-containing compounds (e.g., antimony oxides, selenium oxides, and antimony/selenium impurity phases).[53] This confirms that the synthesized Sb_2Se_3 NWs exhibit a high crystalline quality. These findings lay a foundation for fabricating polarized photodetectors based on Sb_2Se_3 NWs.

The Raman signal is highly sensitive to the chemical bond vibrations and the crystal orientation.[31,32,44,53] Thus, angle-resolved polarized Raman spectroscopy has been previously employed to characterize the anisotropic behavior of materials such as GeSe, $ReSe_2$, and black phosphorus.[31,32,44,53] In this experiment, angle-resolved polarized Raman measurements were performed on Sb_2Se_3 NWs by using a linearly polarized 532 nm laser source. As shown in Figure S7a, the polarization angle θ is defined as the angle between the polarization direction of the incident Raman light and the NW's radial direction (i.e., the ⟨001⟩ lattice direction). Additionally, Raman scattering light in the parallel configuration was utilized for the measurements. The Raman spectra with polarized angles ranging from 0° to 360° (in 20° steps) are presented in Figure S7b. A detailed study of the Raman spectra at polarization angles of 0°, 45°, and 90° is presented in Figure 1g. At 0°, A_g mode peaks of Sb_2Se_3 (101 cm^{-1}, 118 cm^{-1},185 cm^{-1}, 211 cm^{-1}) are distinctly prominent. As the angle increases, A_g peaks weakens significantly at 45° and vanishes entirely at 90°, leaving only two faint B_{3g} modes (109 cm^{-1}, 153 cm^{-1}). To illustrate this phenomenon more clearly, Figure 1h provides a contour color plot of the Raman intensity across all polarization angles. It is evident that the intensity of the A_g mode exhibits a periodic enhancement or diminishment as the polarization angle θ changes. The relationship between the strongest A_g modes (185 cm^{-1} and 211 cm^{-1}) and the varying polarization angle θ is plotted in polar coordinates and is presented in Figures 1i and S7c. The experimental data are effectively fitted using eq 5 in the Supporting Information (see the Supporting Information for the detailed derivation of fitting formulas). The fitting curves for the intensities of both the 185 cm^{-1} and 211 cm^{-1} modes exhibit a butterfly shaped 2-fold symmetry, with the maximum intensity observed at 0° and 180°, and the minimum at 90° and 270°. These Raman results confirm the anisotropic behavior of the crystal structure in our as-grown Sb_2Se_3 NWs, which is in excellent agreement with previous reports.[13,29,31,32]

PbS quantum dots (QDs) were synthesized, employed a hot-injection approach conducted in an oil bath, which is detailed in the Experiment Section.[39,56,57] It should be noted that due to the quantum confinement effect, the bandgap of PbS QDs exhibits a size-dependent relationship described by the following empirical formula[58]

$$E_g = 0.41 + \frac{1}{0.0252d^2 + 0.283d} \qquad (1)$$

This implies that the larger the diameter of the PbS QDs, the narrower their bandgap.[35−37,59,60] Therefore, in the synthesis of PbS QDs in this experiment, the holding temperature and time were appropriately increased to obtain larger-diameter PbS QDs, allowing their absorption wavelength to cover the 1550 nm range.[36−38] Figure S8a shows the scanning transmission electron microscopy (STEM) image of the PbS QDs, in which a large number of QDs with uniform diameters are observed. Figure S8b−d presents the EDS elemental mapping of these QDs, confirming that the QDs consist of Pb and S elements. Figure S8e shows the size distribution histogram of 100 randomly selected PbS QDs, which follows a typical normal distribution with an average diameter of 5.97 nm. To determine the absorption wavelength of the as-synthesized PbS QDs, optical absorption spectroscopy measurements were conducted. During PbS QDs synthesis, their surfaces are typically capped with long-chain ligands (oleic acid) to ensure uniform diameter distribution and suppress aggregation in solution (denoted as PbS-OA).[36,37] However, these long-chain ligands may hinder charge injection at the heterojunction interface.[61] Thus, ligand exchange with short-chain ligands is commonly performed to improve carrier transport efficiency.[35,36,56,60] In this work, a one-step short-chain ligand exchange was carried out using a 1,2-ethanedithiol (EDT)/acetonitrile solution (denoted as PbS-EDT).[38] Detailed experimental procedures are provided in the Experimental Section. The optical absorption spectroscopy results are shown in Figure S8f: after short-chain ligand exchange, the absorption peak exhibits a red shift (from 1425 to 1470 nm), and the absorption wavelength of PbS-EDT QDs cuts off at approximately 1.55 μm. To further investigate the optoelectronic properties of PbS QDs, the PbS-EDT QDs film-based PD was fabricated, as shown in Figure S8g. Measurements reveal that the device exhibits stable photoresponses to 1.31 and 1.55 μm incident light, with $I-T$ curves presented in Figure S8h−i. These results are in excellent agreement with the absorption spectrum of PbS-EDT QDs.

The PbS-EDT QDs were used to form heterojunctions with Sb_2Se_3 NWs and fabricate polarized PD devices. The fabrication process of the heterojunction is illustrated in Figure 2a. Detailed experimental procedures, such as QDs spin-coating, QDs ligand exchange, and NWs transfer, are provided in the Experimental Section. Figure 2b presents the STEM and HRTEM images of PbS QDs, where the measured interplanar spacing of 0.345 nm corresponds to the (111) lattice plane of cubic PbS.[62] Figure 2c shows the HRTEM images of the Sb_2Se_3/PbS heterojunction. It is evident that a QD are attached to the surface of a NW, and the measured interplanar spacings are fully consistent with those of PbS QD and Sb_2Se_3 NW described earlier—confirming the formation of the Sb_2Se_3/PbS 1D-0D mixed-dimensional heterojunction. As detailed in the Experimental Section, the Sb_2Se_3/PbS heterojunctions were subsequently fabricated into PDs. For control experiments, pure Sb_2Se_3 NWs were also fabricated into the PDs. Five groups of PDs based on Sb_2Se_3/PbS heterojunctions and pure Sb_2Se_3 NWs (with comparable shapes and sizes) were selected for comparative testing. Their optical photographs are displayed in Figure S9, where D1, D2, D3, D4, and D5 correspond to the Sb_2Se_3/PbS heterojunction-based PDs, and D1′, D2′, D3′, D4′, and D5′ refer to the pure Sb_2Se_3 NW-based PDs.

Figure 2d presents a schematic of the photoresponse performance measurements of the heterojunction PD under polarized light illumination. In Figures 2e,f and S12a−c, the measurement results for all five sets of devices reveal that in comparison with pure Sb_2Se_3 NW-based PDs, the Sb_2Se_3/PbS heterojunction-based PDs exhibit an obvious enhancement in the photocurrent on/off ratio. More notably, the pure Sb_2Se_3 NW-based PDs show almost no photoresponse in the 1.31 and 1.55 μm wavelengths, which is consistent with previous literature reports.[13,27,33,63,64] In contrast, the Sb_2Se_3/PbS heterojunction-based PDs demonstrate excellent photoresponse at these two wavelengths, indicating that photogenerated carriers from the PbS QDs are efficiently injected into the Sb_2Se_3 NWs, thus extending the photodetection wavelength range. What's more, polarized photoresponse measurements were performed on the Sb_2Se_3/PbS-heterojunction PDs. The testing method for polarization photoresponse is consistent with that reported in our previous work.[10,65] Linearly polarized light is irradiated vertically onto the device with the incident polarized light rotated in 20° steps. To better elucidate the anisotropic photoresponse properties, the polarized photocurrent I_{po} is defined as[10,65]

$$I_{po} = I_{ph}(\theta) - I_{dark} \tag{2}$$

θ is the polarization angle, denoting the angle between the polarization direction of the incident linearly polarized light and the radial direction of the NW, as illustrated schematically in Figure S10. The relationship between the I_{po} of device D2 and the polarization angle θ of the 1.55 μm incident laser is presented in Figure 2g, and that of device D5 is shown in Figure 2h. Both exhibit a sinusoidal relationship, with fitted curves to the experimental data provided in the Figures. The values of I_{po} reach maximum at polarization angles of $\theta = 0°$ and 180°, and minimum values at $\theta = 90°$ and 270°. The other Sb_2Se_3/PbS heterojunction-based PDs, device D1, D3, and D4, exhibit identical polarization performance with respect to the 1.55 μm polarized laser in Figure S11d−f. These results provide conclusive evidence that the polarization detection wavelength of the Sb_2Se_3 NW has been extended to the 1.55 μm range through the formation of the Sb_2Se_3 NW/PbS QDs 1D-0D mixed-dimensional heterojunction. In the following sections, Device D2 is selected for an in-depth investigation of both its conventional and polarized photodetection performances.

Figure S12a is the SEM image of device D2, the diameter of the Sb_2Se_3/ PbS heterojunction is approximately 1 μm, and the device channel is 8 μm. $I-V$ curves of D2 are measured under the visible and near-infrared monochromatic lasers, 520 nm, 915 nm, 1.31, and 1.55 μm. The incident laser's power intensity was calibrated to 0.25 mW/mm^2. From these $I-V$ curves, photocurrents are enhanced relative to the dark current indicating that the Sb_2Se_3/PbS-heterojunction PD exhibits the excellent photoresponse to both visible and near-infrared light. There is a vital parameter for PDs, responsivity (R_λ), which can be computed by the following equation[66−72]

$$R_\lambda = \frac{\Delta I}{(P \times S)} = \frac{I_{ph} - I_{dark}}{P \times S} \tag{3}$$

Here, P denotes the optical power density of the incident laser, I_{ph} the photocurrent, and S the area of PD. R_λ can thus be calculated using these parameters. Under a 3 V bias and an incident laser power density of 0.25 mW/mm^2, the R_λ values are 5.66 A/W for the 520 nm laser, 14.33 A/W for the 915 nm laser, 0.50 A/W for the 1.31 μm laser, and 0.47 A/W for the 1.55 μm laser.

Subsequently, photoresponse performances of the device D2 are analyzed in detail at the wavelengths of 1.55 μm, 1.31 μm, 915 nm, and 520 nm. Figure S12d is the $I_{ph}-P$ curve of D2 under the illumination of 1.55 μm laser, where a gradual slowdown in the increasement of photocurrent with experiment data fitting a power law: $I_{ph}-P^{018}$. Figure S12e is $I-t$ curves under a 3 V bias, with 1.55 μm laser irradiation at different power densities of 0.25, 0.5, and 1 mW/mm^2. These $I-t$ profiles rise to the "on" state and recover to the "off" state as the incident laser is cyclically switched on and off. For 1.31 μm laser, the $I_{Ph}-P$ curve could be fitted as $I_{Ph}-P^{021}$ in Figure S12g, which is consistent with the trend observed under 1.55 μm light illumination. Similarly, $I-t$ curves for the 1.31 μm laser in Figure S12h exhibit characteristics comparable to those of the 1550 nm counterpart. The values of R_λ are calculated using eq 3 above and plotted as 2D contour images: Figure S12f shows the relationship versus bias voltage and 1.55 μm light power density, while Figure S12i presents that versus bias voltage and 1.31 μm light power density. At specific voltage bias, it is observed that the R_λ value is higher when the incident light power intensity is lower. This can be attributed to the nonlinear relationship between the photocurrent and the light power intensity—specifically, $I_{ph}-P^{0.18}$ for 1.55 μm and $I_{ph}-P^{0.21}$ for 1.31 μm—implying a steeper slope in the low-power region of these curves. Specific detectivity (D^*) is another vital characteristic for PDs, which can be calculated using the following equation:[66−72]

$$\text{NEP} = \frac{\text{INC}}{R_\lambda} \tag{4}$$

$$D^* = \frac{(S\Delta f)^{1/2}}{\text{NEP}} = R_\lambda \frac{(S\Delta f)^{1/2}}{\text{INC}} \tag{5}$$

Here, NEP is noise equivalent power, which represents the minimum impinging power to get a signal-to-noise ratio of 1 in a 1 Hz bandwidth. Δf is the response bandwidth. The NEP can be derived from the incident noise current (INC), with the INC data presented in Figure S12c. The 1−10 Hz low-frequency noise, closely related to material defects and device process quality, was selected to calculate D^*. The computed R_λ and D^* values for the 1.55 μm laser are summarized in Table S2, while the corresponding values for the 1.31 μm laser are compiled in Table S3. Under the bias voltage of 3 V, the maximum R_λ and D^* reached 0.86 A/W and 3.33×10^8 cm·Hz$^{1/2}$·W^{1-} for 1.55 μm laser, and 1.12 A/W and 4.30×10^8 cm·Hz$^{1/2}$·W^{1-} for 1.31 μm laser.

Figure S13 is photoresponse properties of the device for 915 and 520 nm incident lasers. Figure S13a is the $I_{ph}-P$ curve for 915 nm incident laser, where the experiment data can be fitted as $I_{ph}-P^{0.63}$, with the functional trend beginning to tend toward linearity. Figure S13b shows $I-t$ curves under a 3 V bias, with 915 nm light intensity of 0.025, 0.5, and 0.75 mW/mm^2. These $I-t$ profiles also rise to the "on" state and recover to the "off" state as the incident 915 nm laser is turned on and off cyclically. Figure S13d shows the $I_{ph}-P$ curve for a 520 nm incident laser, whose functional relationship stands in striking contrast to those observed in the infrared region. The experimental data can be fitted in segments: a nonlinear relationship is observed in the low light intensity region (below 0.08 mW/mm^2), fitting to $I_{ph}-P^{0.36}$, while a linear relationship is noted exists in the high intensity region (above 0.08 mW/mm^2), with the fit expressed as $I_{ph}-2.37 \times 10^{-8}\ P$. Figure S13e is the $I-t$ curves for a 520 nm laser under a 3 V bias, which exhibits the same behavior as that observed under 915 nm laser illumination. The 2D contour images of calculated R_λ for 915 and 520 nm incident lasers are plotted in Figure S13c,f. The higher values of R_λ are also in the lower intensity region. The computed R_λ and D^* values for the 915 nm laser are summarized in Table S4, while the corresponding values for

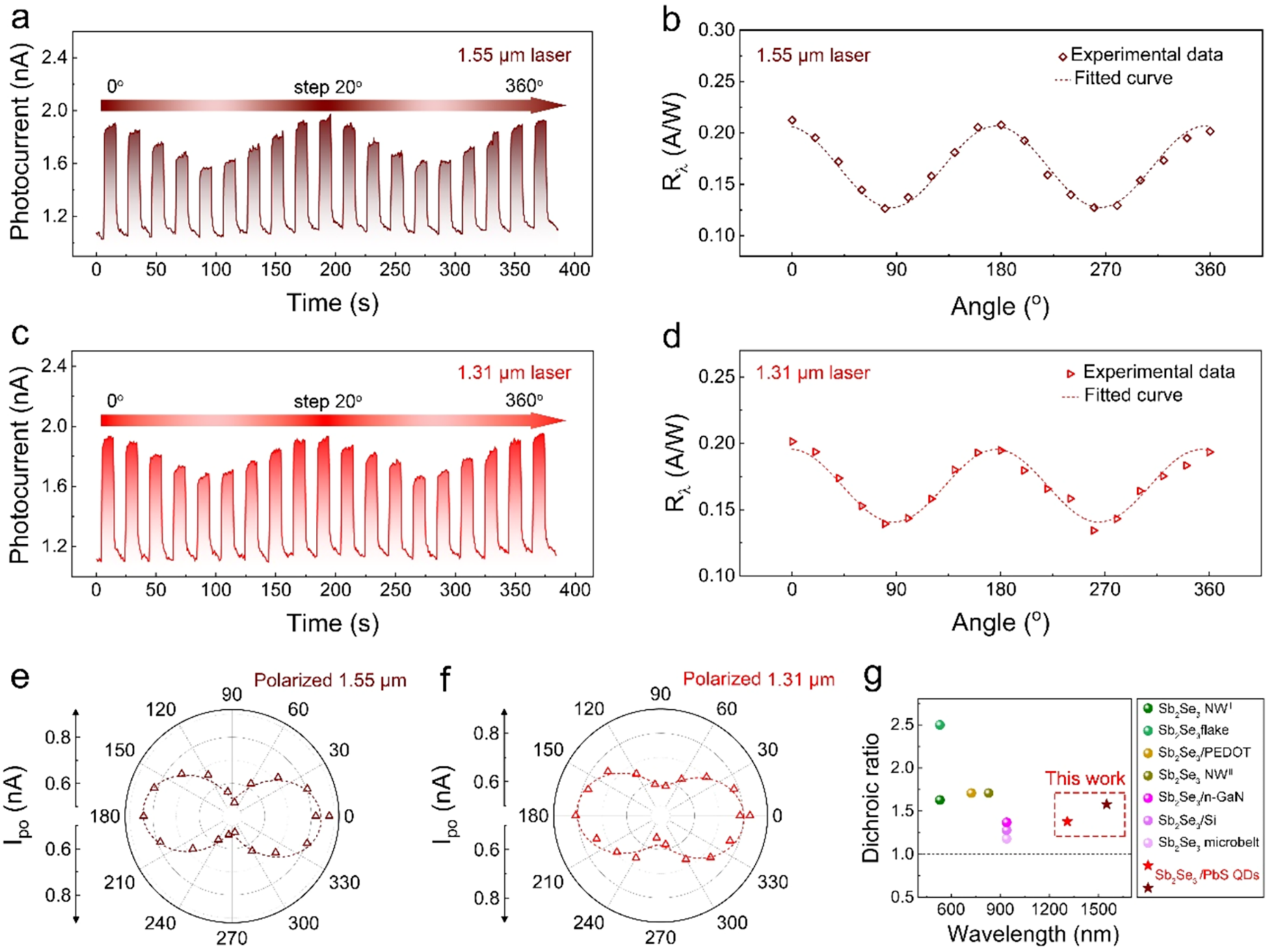

Figure 3. Polarized photoresponses of the Sb_2Se_3/PbS heterojunction-based PD. (a) Time-resolved photoresponse under 1.55 μm linearly polarized laser with polarized angle θ scanned from 0° to 360° in 20° increments. (b) Polarization angle-dependent R_λ to 1.55 μm laser. (c) Time-resolved photoresponse under 1.31 μm linearly polarized laser with polarized angle θ scanned from 0° to 360° in 20° increments. (d) Polarization angle-dependent R_λ to 1.31 μm laser. (e, f) Evolution of the I_{po} with the polarized angle θ of 1.55 and 1.31 μm laser. (g) Comparison of dichroic ratios between the Sb_2Se_3/PbS-based polarization PD in this work and other Sb_2Se_3 structure-based PD.

the 520 nm laser are compiled in Table S5. Under the bias voltage of 3 V, the maximum R_λ and D^* reached 67.54 A/W and 2.60×10^{10} cm·$Hz^{1/2}$·W^{1-} for the 915 nm laser, and 76.60 A/W and 2.95×10^{10} cm·$Hz^{1/2}$·W^{1-} for the 520 nm laser. More importantly, the rise/decay time (t_r/t_d), defined as the time required for the photocurrent to increase from 10% to 90% and decrease from 90% to 10% of its maximum value, is another key parameter for photodetectors. As presented in Figure S14, the device exhibits rise/decay times of 53 μs/54 μs under a 520 nm incident laser, 720 μs/160 μs under a 915 nm incident laser, and 900 μs/400 μs under a 1.55 μm incident laser.

The anisotropic photoresponse properties of D2 are presented in Figure 3, which are characterized using linearly polarized light. For optimal polarized photoelectric response, the input voltage was fixed at 3 V, while the power intensity of incident polarized light was fixed at 0.5 mW/mm^2 for 1.55 and 1.31 μm, and 0.25 mW/mm^2 for 915 and 520 nm. Figure 3a presents the $I-t$ characteristic curve measured under 1.55 μm laser illumination, with polarization angles ranging from 0 ° to 360 ° in 20 ° increments. As the polarization angle varies, the $I-t$ curve exhibits stable periodic fluctuations: the maximum and minimum values occur near 0° (180°) and 90° (270°), respectively, with a period of 180°. The variation of $R_\lambda(\theta)$ with different polarization angles can be calculated by using the following equation

$$R_\lambda(\theta) = \frac{I_{po}}{P \times S} \tag{6}$$

Calculated from the values in the $I-t$ curves the variation trend of R_λ with the polarization angle of the 1.55 μm incident laser is plotted in Figure 3b. This trend can be fitted using a sinusoidal function, with maximum and minimum values of 0.22 and 0.13 A/W, respectively. The $I-t$ curve of the 1.31 μm linearly polarized laser, measured with polarization angles spanning 0° to 360° in 20° steps and plotted in Figure 3c, shows a consistent trend with that of the 1.55 μm laser. The R_λ values derived from the 1.31 μm $I-t$ curve, which are fitted with a sinusoidal function in Figure 3d, yield a maximum of 0.20 A/W and a minimum of 0.14 A/W. For the linearly polarized 915 and 520 nm lasers, the $I-t$ curves measured under the aforementioned polarization angle variation conditions are presented in Figure S15a,c, respectively. These curves exhibit the same variation pattern as those of the

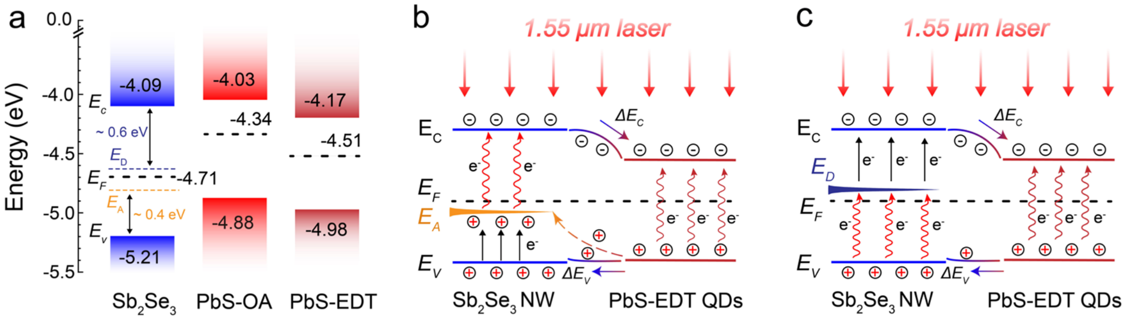

Figure 4. (a) Energy band alignment of Sb_2Se_3 NWs, PbS-OA QDs, and PbS-EDT QDs. (b) PbS QDs-enhanced absorption of 1.55 μm infrared light by the acceptor level (E_A) of Sb_2Se_3 NW. (c) PbS QDs-enhanced absorption of 1.55 μm infrared light by the donor level (E_D) of Sb_2Se_3 NW.

linearly polarized 1.55 and 1.31 μm light. The R_λ values derived from these $I{-}t$ curves were fitted with sinusoidal functions, as shown in Figure S15b,d. For the 915 nm laser, the R_λ values at different polarization angles range from a minimum of 8.9 to a maximum of 12.6 A/W; for the 520 nm laser, the Rλ values at different polarization angles range from a minimum of 6.6 to a maximum of 7.5 A/W.

To more intuitively investigate the anisotropic photoresponse properties, we extracted the angularly resolved photocurrents from the aforementioned $I{-}t$ curves and plotted them as angle-dependent polar graphs. In Figure 3e,f and S16, the variation of I_{po} with the incident light polarization angle exhibits a 2-fold symmetry in all cases: the maximum I_{po} is achieved when the incident light is parallel to the radial direction of the NW ($\theta = 0°$, 180°), whereas the minimum I_{po} is recorded when the incident light is perpendicular to the radial direction of the NW ($\theta = 90°$, 270°). The variation pattern of I_{po} can be fitted by the following mathematical expression[10,12,73,74]

$$I_{po}(\theta) = I_{pox}\cos^2(\theta + \varphi) + I_{poy}\sin^2(\theta + \varphi) \qquad (7)$$

Here, φ serves as an angle correction coefficient. $I_{po}(\theta)$, I_{pox}, and I_{poy} correspond to the theoretical components of I_{po} along the θ direction, y-axis, and x-axis, respectively. The dichroic ratio (I_{poy}/I_{pox}) can be calculated from the measurement results, with values of 1.58 under the 1.55 μm laser, 1.38 under the 1.31 μm laser, 1.33 under the 915 nm laser, and 1.10 under the 520 nm laser, respectively. Figure 3g presents a statistical comparison of dichroic ratios between the Sb_2Se_3/PbS heterojunction-based polarized PD in this work and other Sb_2Se_3 structure-based polarized PDs reported in the literature. More detailed data are provided in Table S5. Since the bandgap of Sb_2Se_3 synthesized via various methods ranges from 1.0 to 1.3 eV, to date, all reported polarization response wavelengths of Sb_2Se_3 lie below 1000 nm.[13,27,28,31,33,34,75] In this work, through forming heterojunctions between Sb_2Se_3 NW and PbS QDs, we successfully extended polarization detection wavelengths to infrared 1.31 and 1.55 μm, while maintaining a dichroic ratio and R_λ comparable to those reported in the literature.

Through the analysis of UPS and PL measurement results in Figure S17, the precise energy band alignments of Sb_2Se_3 NWs, PbS-OA QDs, and PbS-EDT QDs relative to the vacuum level are illustrated in Figure 4a.[76,77] The Fermi levels E_F of these three materials are −4.71 eV, −4.34 eV, and − 4.51 eV, with their corresponding bandgaps are 1.12, 0.85, and 0.81 eV. Specific values for the valence band maximum (E_V) and conduction band minimum (E_C) are also explicitly labeled in the figure. In this work, a heterojunction is formed between the Sb_2Se_3 NW and PbS-EDT QD to fabricate the polarized photodetector. After contact, the energy band structure at the heterojunction interface is depicted in Figure 4b,c, where the conduction band offset ΔE_C is 0.28 eV and the valence band offset ΔE_V is 0.02 eV. This structure corresponds to a quasi-type-II heterojunction configuration, which can effectively promote the separation of photogenerated carriers, and thereby enhancing the photoresponse performance.[21,78,79] According to the literature, the as-synthesized PbS QDs in this work exhibit a cuboctahedral structure with Pb-rich (111) facets and Pb−S (100) facets.[80] However, based on the diameter statistics presented in Figure S8e, the PbS QDs do not exhibit monodispersity.[81] Even though individual QD may exhibit anisotropic light absorption characteristics, a large ensemble of QDs with varying diameters and random orientations fails to demonstrate the light absorption behavior of a single QD. As illustrated in Figure S18a, three PbS QDs are visible within a 100 nm range along the Sb_2Se_3 NW. Within the 8 μm channel length of the Sb_2Se_3 NW/PbS QDs heterojunction-based PD, a greater number of PbS QDs are distributed on the NW surface. To support this argument, the polarization photoresponse of a PbS QDs film-based PD was characterized. As shown in Figure S18c, under 1.55 μm incident light with different polarization angles, the $I{-}T$ curve exhibits no distinct variation trend. Therefore, the anisotropic photoresponse of the heterojunction device to the 1.55 μm laser arises from another mechanism. According to literature reports, there are three main defect energy levels in Sb_2Se_3: a donor level (E_D) located 0.6 eV below the E_C and two acceptor levels (E_A) situated 0.4 and 0.7 eV above the E_V.[82−86] These defect energy levels can induce an extrinsic photoresponse to infrared light; for instance, Li et al. reported that the responsivity of Sb_2Se_3-based PD to 1.55 μm infrared light is 0.042 $mA{\cdot}W^{-1}$.[85] This is consistent with our observation in Figure S11a,c, where pure Sb_2Se_3 NW-based-PDs show a weak photoresponse to 1.55 μm light.

To simplify the analytical model, we focus here on the absorption of infrared light by the E_A below the E_F and the E_D above the E_F of Sb_2Se_3 NW. As shown in Figure 4b, under illumination with 1.55 μm infrared light, electrons trapped by the E_A of Sb_2Se_3 NW from the E_V can be excited to the E_C. Owing to the type-II heterojunction effect, photogenerated carriers separate at the interface between Sb_2Se_3 NW and PbS QDs: electrons transfer from the E_C of Sb_2Se_3 NW to that of PbS QDs, while holes migrate not only from the E_V of PbS QDs to the E_V of Sb_2Se_3 NW but also to the E_A of Sb_2Se_3 NW.[21,78,79] This facilitates the E_A of the Sb_2Se_3 NW to further

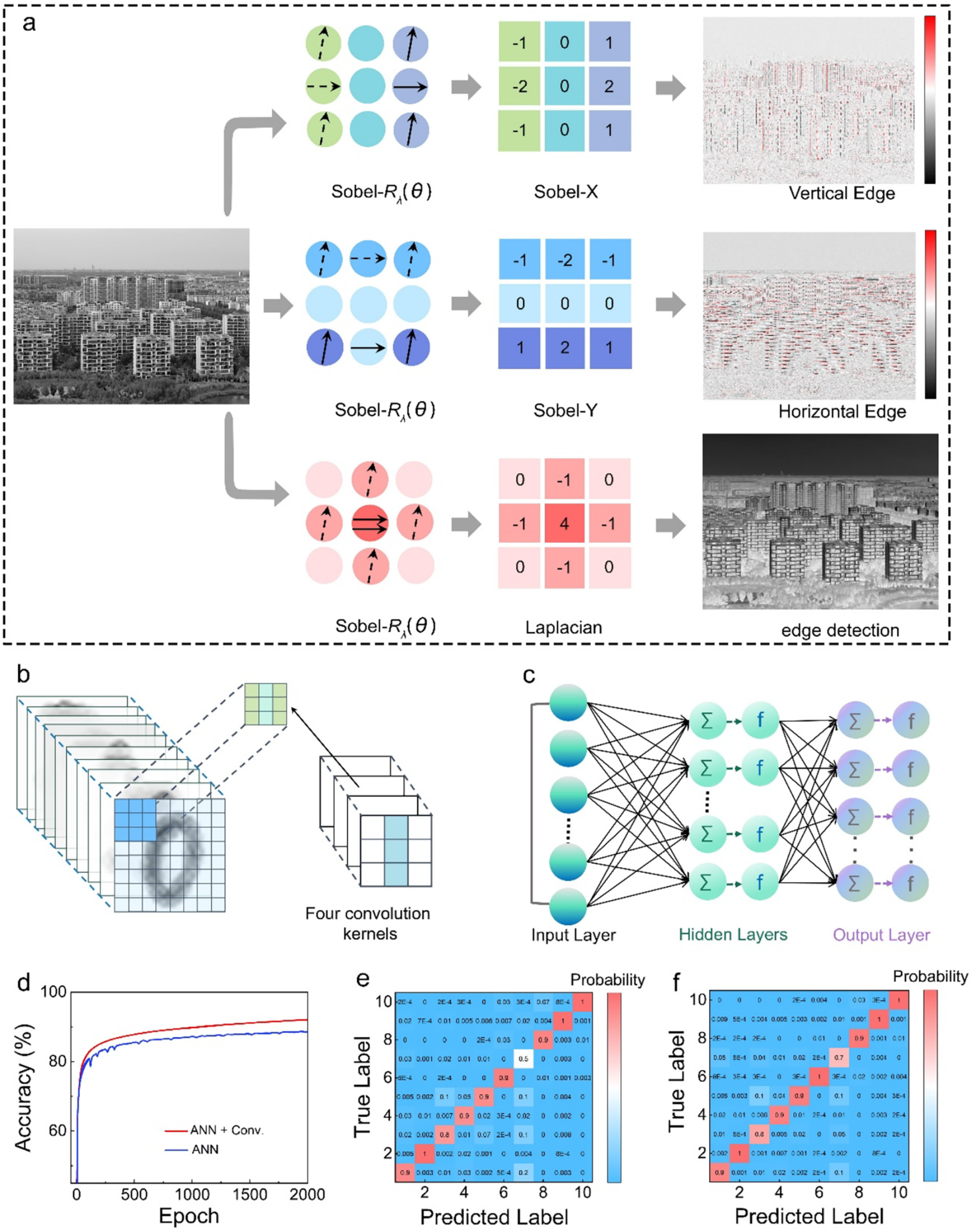

Figure 5. Image feature extraction and recognition with convolutional kernels based on the infrared polarization detection performance of the Sb_2Se_3/PbS-heterojunction PD. (a) Implementation of the Sobel-X, Sobel-Y, and Laplacian for feature extraction of input original landscape images under vertical, horizontal, and edge modes, respectively. (b) Schematic of artificial visual preprocessing with 4-fold convolutional kernels, and (c) schematic of a three-layer artificial neural network (ANN). (d) Recognition accuracy of the ANN under conditions with and without the convolutions. (e, f) Classification results from the confusion matrix for the ANN without and with convolution kernels.

trap electrons from the E_V, sustaining the photoresponse. Figure 4c presents the analysis of the type-II heterojunction-enhanced infrared light absorption by the E_D of the Sb_2Se_3 NW. Upon absorption of incident photons by the Sb_2Se_3 NW, electrons are excited from the E_V to the E_D, followed by their transition to the E_C. Since electrons transfer from the E_C of Sb_2Se_3 NW to that of PbS QDs, the transition of electrons from the E_D to the E_C is further promoted, thereby enhancing the photoresponse of the E_D in Sb_2Se_3 NW to 1.55 μm incident light. Consequently, the type-II heterojunction effect between the Sb_2Se_3 NW and PbS QDs significantly enhances the extrinsic photoresponse of the Sb_2Se_3 NW to incident infrared light. To confirm this analysis, the incident laser of 1.645 μm (0.75 eV) was employed for the study, with its energy lower than the bandgap of PbS-EDT QDs but enough to excite electrons from the E_V to E_D in Sb_2Se_3 NW. As presented in Figure S19, the pure Sb_2Se_3 NW-based PD exhibits almost no photoresponse to 1.645 μm infrared light, whereas the Sb_2Se_3/PbS heterojunction-based PD shows a distinct photoresponse to this wavelength. This further verifies that the photoactivation of PbS-EDT QDs enables trap-assisted absorption in the Sb_2Se_3 NW. The responsivity of the Sb_2Se_3/PbS heterojunction-based PD measured in this work to 1.55 μm infrared light is 0.86 A/W, which is much higher than the 0.042 mA/W of Sb_2Se_3 PD reported in the literature.[85] Finally, due to the anisotropic light absorption property of Sb_2Se_3 NW, the polarization detection wavelength of the Sb_2Se_3/PbS heterojunction-based PD is extended to 1.55 μm.

Direct photocurrent calculation enables in-sensor convolution computing and subsequent image processing tasks, leveraging Kirchhoff's Current Law (KCL) and the photocurrent generation process, where the relationship $I_{po} \propto P \times R_\lambda$ is derived from eq 7.[87−89] Owing to the strong correlation between the R_λ of the Sb_2Se_3/PbS heterojunction-based PD and the polarization angle of 1.55 μm incident laser, we can assign R_λ weights to different 3 × 3 convolution kernels by adjusting the polarization angle, thereby accomplishing the task of image edge feature extraction. As shown in Figure 5a, we construct the Sobel-X, Sobel-Y, and Laplacian convolution kernels based on the polarization $R_\lambda(\theta)$ for 1.55 μm light of the device. Convolution kernels were then used to perform averaging, first derivative and second derivative operations on the image to achieve smoothing and sharpening operations, thereby realizing the extraction of x-direction, y-direction, and edge features of the image.[88−90] The specific numerical values corresponding to the operator symbols in the figure are listed in Table S7. Through software simulation, we multiply the R_λ at polarization angles of 0° and 80° by the optical signals corresponding to the pixels of the original image, followed by summation. This yields edge-extracted images, enabling the completion of image processing tasks, including horizontal edge detection, vertical edge detection, and general edge detection, respectively. As can be seen from the results, compared with the original image, the vertical and horizontal features of the building in the feature-extracted image are sharpened and the edge feature information is also significantly enhanced. In addition, convolution kernels for 45° and 135° edge detection are constructed, as shown in Figure S20, enabling the processing of 45° and 135° edge information from the original image.

To evaluate the improvement of image recognition enabled by edge feature extraction via in-sensor computing, in Figure 5b four 3 × 3 convolution kernels, corresponding to the aforementioned X, 45°, Y, and 135° operators, are constructed to process images from the Fashion-MNIST data set. Subsequently, the four extracted edge feature results are fused and fed into a three-layer artificial neural network (ANN), whose structural schematic is illustrated in Figure 5c. As shown in Figure 5d, the ANN with the integrated convolution kernels exhibits higher recognition accuracy; specifically, the recognition accuracy of the device is improved from 88% to 92%. This demonstrates the crucial role of the convolution kernels in effectively extracting edge features. Furthermore, during the training process of the ANN, the confusion matrix is significant for evaluating the performance of the classifier. Consequently, it is used to investigate the classification learning task. Figure 5e,5f, respectively, presents the classification results from the confusion matrices—corresponding to posttraining feature extraction without convolution kernels and with convolution kernels. Taking Sneakers (a class in the data set) as an example, the classification accuracy increased from 0.5 to 0.7 before and after incorporating convolution kernels for feature extraction. These results indicate that in the present work, the ANN preprocessing using convolution kernels, which is constructed from the infrared polarization detection performance of the Sb_2Se_3/PbS-heterojunction PD, can effectively extract relevant feature information, reduce redundant data and noise, and facilitate the image recognition process.

■ CONCLUSIONS

In summary, intrinsic anisotropic Sb_2Se_3 NWs were grown via the CVD method, and PbS QDs were synthesized through a liquid-phase procedure. Sb_2Se_3 NW/PbS QD heterojunctions were constructed with interfacial photogenerated carrier transport enhanced via long-to-short-chain ligand exchange. Compared with pure Sb_2Se_3 NW-based PDs, the Sb_2Se_3/PbS heterojunction-based PDs exhibit enhanced photoelectric detection performance: not only are their detection wavelengths extended to 1.55 μm but, more impressively, their polarization detection wavelengths are also extended to 1.55 μm. The Sb_2Se_3/PbS heterojunction-based PD demonstrates excellent photoresponse performance. Specifically, for 915 nm, 1.31 μm, and 1.55 μm lasers, its R_λ reaches 67.54 A/W, 1.12 A/W, and 0.86 A/W, respectively, while the D^* are 2.60×10^{10} $\mathrm{cm \cdot Hz^{1/2} \cdot W^{1-}}$, 4.30×10^{8} $\mathrm{cm \cdot Hz^{1}/^{2} \cdot W^{1-}}$, and 3.33×10^{8} $\mathrm{cm \cdot Hz^{1}/^{2} \cdot W^{1-}}$. The measured dichroic ratios for polarized light at these three wavelengths are 1.33, 1.38, and 1.58. Analyses of UPS and PL data reveal that a quasi-type-II band alignment is formed at the Sb_2Se_3/PbS heterojunction interface. The separation of photogenerated carriers at this heterojunction interface enhances the absorption of infrared polarized light by the defect energy levels in the Sb_2Se_3 NWs, thereby extending the polarized photoresponse wavelength to 1.55 μm. Additionally, five convolution kernels were constructed from the polarization-dependent R_λ values of the heterojunction PD with 1.55 μm light. Employing these convolution kernels, the ANN can effectively extract relevant feature information, reduce redundant data and noise, and facilitate image recognition. These exceptional polarization detection properties of Sb_2Se_3/PbS-heterojunction PDs confirm that QDs coupling to extend infrared polarization detection is an innovative and reliable approach with significant potential for further developments and applications.

■ EXPERIMENTAL SECTION

Theoretical Calculation

The lattice constants of relaxed Sb_2Se_3 are as follows: a = 11.62 Å, b = 11.77 Å, and c = 3.962 Å. As shown in Figure S1, the unit cell of Sb_2Se_3 can be visualized using the VESTA software.[42] First-principles calculations were carried out based on density functional theory (DFT) using the Vienna ab initio simulation package (VASP).[45] The projector augmented wave (PAW) method was used to describe the core electrons.[46] The generalized gradient approximation (GGA) with the Perdew−Burke−Ernzerhof (PBE) functional was adopted to treat the exchange-correlation potential,[47,48] and the HSE06 (Heyd-Scuseria-Ernzerhof) hybrid functional was used to obtain more accurate electronic band structures.[49] A kinetic energy cutoff of 500 eV and a Monkhorst−Pack k-mesh of 8 × 3 × 3 sampling in the full Brillouin zone were used in our calculations. The structures were optimized until all residual forces on each atom were less than 0.01 eV/Å. The simulations were performed at 0 K.

https://doi.org/10.1021/acsnano.5c16680

Synthesis of Sb_2Se_3 NWs and PbS QDs

Schematic diagram of Sb_2Se_3 NWs grown by the CVD method is shown in Figure S2. To accelerate the flow rate of the precursor, a small, thin tube was inserted into the horizontal quartz tube furnace. Commercially available Sb_2Se_3 powder was placed in the center of the heating zone. Monocrystalline silicon wafers or SiO_2 wafers coated with a 3 nm Au film were used as growth substrates and placed in the downstream region of the furnace. The quartz tube was evacuated, and a 9:1 argon−hydrogen mixture at a flow rate of 170 sccm was used as the carrier gas. The temperature at the heating center was raised to 750 °C within 20 min, and meanwhile, the growth region reached about 450 °C. After maintaining the temperature for 30 min, the system was naturally cooled to room temperature. A large number of nanowires were found to have grown on the substrate.

The synthesis of Oleic acid-capped PbS QDs was adapted from previously reported methods that employed a hot-injection approach conducted in an oil bath.[35,37,56,57] Our experimental setup is depicted in Figure S3. 0.36 g of lead oxide (PbO), 1 mL of oleic acid (OA), and 15 mL of octadecene (ODE) were mixed under magnetic stirring and heated to 140 °C for 1 h under a nitrogen atmosphere, yielding a transparent colorless solution. Then 4.0 mL of the ODE containing 100 μL of bis(trimethylsilyl) sulfide (TMS) was swiftly injected into the reaction flask, followed by maintaining the temperature at 120 °C for 1 h. After the mixture was naturally cooled to room temperature, the purification procedure was carried out as follows: First, acetone was added to the solution, which was then centrifuged at 1500 rpm for 10 min. The supernatant was discarded, and an appropriate amount of toluene was added to dissolve the product thoroughly. This process was repeated 2−3 times to obtain a pure black colloidal solution of PbS in toluene. Subsequently, the PbS-toluene solution was dried using a vacuum drying oven to yield a quantum dot powder. Finally, the PbS-OA QDs were dispersed in *n*-octane to prepare a 50 mg/mL *n*-octane solution.

Short-Chain Ligand Exchange of PbS QDs

PbS-OA QDs were uniformly spin-coated onto SiO_2 or FTO glass substrates. A 10 vol % solution of ethanedithiol (EDT) in acetonitrile was drop-cast onto the surface, allowed to react for 1 min, and then spun at 1200 rpm for 10 s. The substrate was then gently rinsed with acetonitrile to remove excess ligands. This ligand exchange cycle was repeated three times to yield uniform PbS-EDT QDs films. The PbS-EDT QDs films prepared via this method were used for the PL and UPS measurements.

Material Characterization

The morphological features and crystallographic phases were examined by using scanning electron microscopy (SEM, Hitachi S4800) and aberration-corrected high-resolution transmission electron microscopy (HRTEM, JEOL ARM200F). Elemental composition and chemical valence states were determined via X-ray diffraction (XRD, D8 ADVANCE, Bruker) and X-ray photoelectron spectroscopy (XPS, Escalab 250Xi, Thermo Fisher Scientific). Angle-resolved Raman spectra of Sb_2Se_3 were acquired using a microscopic confocal laser Raman spectrometer (InVia, Renishaw, excited by the 532 nm laser). Microphotoluminescence (PL) measurement of Sb_2Se_3 NWs was performed using a Jobin-Yvon HR800 system. The photoluminescence (PL) measurement of PbS QDs was performed using a homemade mid-infrared fluorescence measurement system.

Fabrication of Sb_2Se_3/PbS Heterojunctions-Based Photodetectors

The fabrication process is illustrated in Figure 2a. ① Oleic acid-capped PbS QDs (25 mg/mL) were spin-coated onto the sample with pregrown Sb_2Se_3 NWs. After standing for 10 s, the sample was spun at 1500 rpm for 10 s to ensure thorough coverage of Sb_2Se_3 NWs with PbS-OA QDs. ② A 10 vol % solution of ethanedithiol (EDT) in acetonitrile was drop-cast onto the aforementioned sample. After standing for 1 min, the sample was spun at 1200 rpm for 10 s, followed by gentle rinsing with acetonitrile to remove excess ligands. This procedure was repeated more than three times, and the sample was subsequently baked at 75 °C for 15 min under a nitrogen atmosphere. Through these steps, the long-chain OA ligands on the PbS QDs surface were replaced with short-chain EDT ligands. ③ The Sb_2Se_3 /PbS heterojunctions were transferred onto a SiO_2/Si substrate. UV photolithography and thermal evaporation were employed to pattern 15/85 nm thick electrodes. Finally, photodetectors based on Sb_2Se_3/PbS heterojunctions were successfully fabricated.

Optoelectronic Measurements

The photoelectric signals from both the Sb_2Se_3/PbS heterojunction-based PD and the pure Sb_2Se_3 NW-based PD were characterized by using a Keithley B1500A semiconductor analyzer integrated with a probe station. Illumination was provided by semiconductor lasers operating at 520 nm (CNI, MDL-III-520), 915 nm (CNI, MDL-III-915), 1310 nm (CNI, MDL-III-1310), and 1550 nm (CNI, MDL-III-1550). The laser beam was incident directly on the photodetector without focusing, with a measured spot diameter of 0.5 mm. A Newport power meter was used to quantify the incident laser power density, while NEP were recorded via a PDA equipment (Platform Design Automation, Inc.).

The polarized properties of the Sb_2Se_3/PbS heterojunction-based PD were tested using our homemade system, which was a microscopic testing setup incorporating a polarizer (Glan-Taylor prism) and a half-wave plate. The polarization direction of the incident light was modulated by the polarizer and half-wave plate before the devices. The laser sources were also the aforementioned semiconductor lasers, 520, 915, 1310, and 1550 nm. Polarized photoelectric signals are collected by the probe station and transmitted to the B1500A semiconductor analyzer. All measurements were performed under ambient atmospheric conditions at room temperature.

Artificial Neural Network Simulation

A three layers fully connected ANN were constructed in MATLAB, consisting of 2704 input neurons (feature dimensions), 500 hidden neurons (ReLU activation), and 10 output neurons (softmax classification). The input neurons are associated with the feature dimensions of the data set, and the 10 output neurons represent the 10 distinct classes.

■ ASSOCIATED CONTENT

Supporting Information

The Supporting Information is available free of charge at https://pubs.acs.org/doi/10.1021/acsnano.5c16680.

Unit cell of Sb2Se3, orthorhombic system, schematic illustration of the CVD process to grow Sb_2Se_3 NWs, the photograph of the oil bath used for the synthesis of PbS QDs, STEM image of a Sb_2Se_3 NW and corresponding EDS element distribution maps of Sb and Se, the FFT image, the XPS spectra, the Sb_2Se_3 NW used for polarized Raman measurements and the polarized Raman results, the characterization of as-synthesized PbS QDs, the photograph of Sb_2Se_3/PbS-heterojunction PD and pure Sb_2Se_3 NWs PD, the photograph of Sb_2Se_3/PbS-heterojunction polarized PD, the comparison of photoresponse performance between Sb_2Se_3/PbS heterojunction-based photodetectors and pure Sb_2Se_3 NW-based photodetectors, photoresponse properties of Sb_2Se_3/PbS heterojunction-based PD, the polarization photoresponse of Sb_2Se_3/PbS-heterojunction PD, the image feature extraction with convolutional kernels based on the infrared polarization detection performance of the Sb_2Se_3/PbS-heterojunction PD; the four Raman tensors corresponding to crystals with D_{2h} symmetry groups (Table S1); the summary of the R_λ and D^* of the Sb_2Se_3/PbS-heterojunction PD for 1.55 μm, 1.31 μm, 915 and 520 nm (Tables S2−S5); the comparison of key parameters between the Sb_2Se_3/PbS-based polarization photodetector in this work and other Sb_2Se_3 structure-based photodetectors (Table S6); the physical meanings and specific values represented by the operator symbols in the main text (Table S7) (PDF)

■ AUTHOR INFORMATION

Corresponding Authors

Guozhen Shen − *School of Integrated Circuits and Electronics, Beijing Institute of Technology, Beijing 100081, China*; Email: gzshen@bit.edu.cn

Zhongming Wei − *State Key Laboratory of Semiconductor Physics and Chip Technologies, Institute of Semiconductors, Chinese Academy of Sciences, Beijing 100083, China*; Email: zmwei@semi.ac.cn

Haitao Yang − *Institute of Physics, Chinese Academy of Sciences and University of Chinese Academy of Sciences, Beijing 100190, China*; Email: htyang@iphy.ac.cn

Authors

Kai Zhang − *Institute of Physics, Chinese Academy of Sciences and University of Chinese Academy of Sciences, Beijing 100190, China*

Wenhao Ran − *School of Integrated Circuits and Electronics, Beijing Institute of Technology, Beijing 100081, China*

Yali Yu − *School of Physical Science and Engineering, Beijing Jiaotong University, Beijing 100044, China*

Pan Wang − *State Key Laboratory of Semiconductor Physics and Chip Technologies, Institute of Semiconductors, Chinese Academy of Sciences, Beijing 100083, China*

Huichen Cao − *Hebei Key Lab of Optic-electronic Information and Materials, the College of Physics Science and Technology, Hebei University, Baoding 071002, China*

Bin Dai − *Institute of Physics, Chinese Academy of Sciences and University of Chinese Academy of Sciences, Beijing 100190, China*

Yechao Han − *Institute of Physics, Chinese Academy of Sciences and University of Chinese Academy of Sciences, Beijing 100190, China*

Linjuan Guo − *Hebei Key Lab of Optic-electronic Information and Materials, the College of Physics Science and Technology, Hebei University, Baoding 071002, China*

Zhiqiang Li − *Hebei Key Lab of Optic-electronic Information and Materials, the College of Physics Science and Technology, Hebei University, Baoding 071002, China*

Juehan Yang − *State Key Laboratory of Semiconductor Physics and Chip Technologies, Institute of Semiconductors, Chinese Academy of Sciences, Beijing 100083, China*; orcid.org/0000-0002-7379-1080

Hui Guo − *Institute of Physics, Chinese Academy of Sciences and University of Chinese Academy of Sciences, Beijing 100190, China*

Lihong Bao − *Institute of Physics, Chinese Academy of Sciences and University of Chinese Academy of Sciences, Beijing 100190, China*; orcid.org/0000-0002-2942-892X

Hongjun Gao − *Institute of Physics, Chinese Academy of Sciences and University of Chinese Academy of Sciences, Beijing 100190, China*; orcid.org/0000-0002-6766-0623

Complete contact information is available at:
https://pubs.acs.org/10.1021/acsnano.5c16680

Author Contributions

[#]K.Z., W.H.R., and Y.L.Y. contributed equally to this work. Y.L.Y. carried out the measurement of polarization detection performances of device. P.W. performed the DFT calculation. H.C.C. contributed to the growth of Sb_2Se_3 NW. B.D. and Y.C.H. contributed to the synthesis of PbS QDs. L.J.G. performed the SEM measurement. Z.Q.L. and J.H.Y. provided guidance on the analysis of UPS result. H.G. performed the PL measurement. L.H.B. and H.J.G. provided revision comments on the manuscript. The paper was cowritten by K.Z. and W.H.R., G.Z.S., Z.M.W., and H.T.Y. guided the whole project.

Notes

The authors declare no competing financial interest.

■ ACKNOWLEDGMENTS

We acknowledge the financial support from the National Key Research and Development Program of China (2022YFA1204100), the National Natural Science Foundation of China (62488201, 62404017, 62125404, 62461160330, U24A20285), the CAS Superconducting Research Project (SCZX-0101), the Beijing Natural Science Foundation (Z220005), the Postdoctoral Fellowship Program of the China Postdoctoral Science Foundation (GZB20240938, GZB20250150, 25T181112), the Natural Science Foundation of Hebei Province (E2021201043), and the Science and Technology Plan Project of Hebei Province (226Z1002G).

■ REFERENCES

(1) Wei, J.; Xu, C.; Dong, B.; Qiu, C.-W.; Lee, C. Mid-infrared semimetal polarization detectors with configurable polarity transition. *Nat. Photonics* **2021**, *15*, 614−621.

(2) Rigopoulou, D.; S, H. W. W.; Genzel, R.; Lutz, D.; Moorwood, A. F. M.; Tran, Q. D. A large mid-infrared spectroscopic and near-infrared imaging survey of ultraluminous infrared galaxies: their nature and evolution. *Astron. J.* **1999**, *118*, 2625−2645.

(3) Berndt, E. B.; Zavodsky, B. T.; Folmer, M. J. Development and Application of Atmospheric Infrared Sounder Ozone Retrieval Products for Operational Meteorology. *IEEE Trans. Geosci. Electron.* **2016**, *54*, 958−967.

(4) Guo, B.; W, Y.; Peng, C.; Zhang, H. L.; Luo, G. P.; Le, H. Q.; et al. Laser-based mid-infrared reflectance imaging of biological tissues. *Opt. Express* **2004**, *12*, 208−219.

(5) Tyo, J. S.; G, D. L.; Chenault, D. B.; Shaw, J. A. Review of passive imaging polarimetry for remote sensing applications. *Appl. Opt.* **2006**, *45*, 5453−5469.

(6) Zhao, Z.; Liu, J.; Liu, Y.; Zhu, N. High-speed photodetectors in optical communication system. *J. Semicond.* **2017**, *38*, No. 121001.

(7) Tong, L.; Huang, X.; Wang, P.; Ye, L.; Peng, M.; An, L.; Sun, Q.; Zhang, Y.; Yang, G.; Li, Z.; Zhong, F.; Wang, F.; Wang, Y.; Motlag, M.; Wu, W.; Cheng, G. J.; Hu, W. Stable mid-infrared polarization imaging based on quasi-2D tellurium at room temperature. *Nat. Commun.* **2020**, *11*, No. 2308.

(8) Chen, Y.; T, C.; Wang, Z.; Miao, J.; Ge, X.; Zhao, T.; Liao, K.; Ge, H.; Wang, Y.; Wang, F.; Zhou, Y.; Wang, P.; Zhou, X.; Shan, C.; Peng, H.; Hu, W. Momentum-matching and band-alignment van der Waals heterostructures for high-efficiency infrared photodetection. *Sci. Adv.* **2022**, *8*, No. eabq1781.

(9) Xin, K.; Zhou, Z.; Qiu, S.; Liu, T.; Yu, Y.; Yang, J.; Hu, W.; Wei, Z. Low-dimensional low-symmetric semiconductors for polarization-sensitive photodetection. *Nat. Rev. Electr. Eng.* **2025**, *2*, 480−493.

(10) Wang, X.; Li, Y.; Huang, L.; Jiang, X. W.; Jiang, L.; Dong, H.; Wei, Z.; Li, J.; Hu, W. Short-Wave Near-Infrared Linear Dichroism of Two-Dimensional Germanium Selenide. *J. Am. Chem. Soc.* **2017**, *139*, 14976−14982.

(11) Zhao, K.; Yang, J.; Wang, P.; Zhou, Z.; Long, H.; Xin, K.; Liu, C.; Han, Z.; Liu, K.; Wei, Z. β-Ga_2O_3 Nanoribbon with Ultra-High Solar-Blind Ultraviolet Polarization Ratio. *Adv. Mater.* **2024**, *36*, No. 2406559.

(12) Zhao, K.; Yang, J.; Zhong, M.; Gao, Q.; Wang, Y.; Wang, X.; Shen, W.; Hu, C.; Wang, K.; Shen, G.; Li, M.; Wang, J.; Hu, W.; Wei, Z. Direct Polarimetric Image Sensor and Wide Spectral Response Based on Quasi-1D Sb_2S_3 Nanowire. *Adv. Funct. Mater.* **2020**, *31*, No. 2006601.

(13) Yu, P.; Yu, X.; Kong, Y.; Sun, L.; Jiang, Y. Sb_2Se_3 Microbelt/PEDOT Heterojunction for a Self-Powered Visible to Near-Infrared Photodetector with High Polarization-Sensitive Imaging. *ACS Appl. Electron. Mater.* **2025**, *7*, 1684−1693.

(14) Wang, Y.; Lai, Z.; Tang, S.; Wang, J.; Zhou, Q.; Li, S.; Wang, W.; Zhao, H.; Yu, Y.; Gao, L. $ReS_2/MoSe_2$ Van der Waals Heterostructure Photodetectors for Polarization Imaging and Polarization-Encoded Optical Communication. *Small* **2025**, *21*, No. 2503599.

(15) Cheng, J.; Yu, K.; Xu, J.; Zhou, G.; Zhang, Z.; Xiang, H.; Chen, Z. Two-dimensional anisotropic semiconductors: from structure and properties to device applications. *Nanoscale* **2025**, *17*, 15086−15109.

(16) Yu, Y.; Xiong, T.; Guo, Z.; Hou, S.; Yang, J.; Liu, Y.-Y.; Gu, H.; Wei, Z. Wide-spectrum polarization-sensitive and fast-response photodetector based on 2D group IV-VI semiconductor tin selenide. *Fundam. Res.* **2022**, *2*, 985−992.

(17) Wang, Z.; Luo, P.; Han, B.; Zhang, X.; Zhao, S.; Wang, S.; Chen, X.; Wei, L.; Yang, S.; Zhou, X.; Wang, S.; Tao, X.; Zhai, T. Strong In-Plane Anisotropic SiP_2 as a IV−V 2D Semiconductor for Polarized Photodetection. *ACS Nano* **2021**, *15*, 20442−20452.

(18) Li, L.; Yu, Y.; Ye, G. J.; Ge, Q.; Ou, X.; Wu, H.; Feng, D.; Chen, X. H.; Zhang, Y. Black phosphorus field-effect transistors. *Nat. Nanotechnol.* **2014**, *9*, 372−377.

(19) Long, M.; G, A.; Wang, P.; Xia, H.; Ott, C.; Pan, C.; Fu, Y.; Liu, E.; Chen, X.; Lu, W.; Nilges, T.; Xu, J.; Wang, X.; Hu, W.; Miao, F. Room temperature high-detectivity mid-infrared photodetectors based on black arsenic phosphorus. *Sci. Adv.* **2017**, *3*, No. e1700589.

(20) Song, C.; Chen, J.; Ding, X.; Xu, Y.; Xu, H.; Li, H.; Shen, W.; Hu, C.; Zhang, H.; Wang, S.; Yao, J. Ultra-Broadband Polarization-Sensitive O-doped $ZrTe_3$ Photodetector Induced by UV Laser. *Adv. Mater.* **2025**, *37*, No. 2506840.

(21) Reiss, P.; Protière, M.; Li, L. Core/Shell Semiconductor Nanocrystals. *Small* **2009**, *5*, 154−168.

(22) Lo, S. S.; Mirkovic, T.; Chuang, C. H.; Burda, C.; Scholes, G. D. Emergent Properties Resulting from Type-II Band Alignment in Semiconductor Nanoheterostructures. *Adv. Mater.* **2011**, *23*, 180−197.

(23) Liu, F.; Zhuang, X.; Wang, M.; Qi, D.; Dong, S.; Y, S.; Yin, Y.; Zhang, J.; Sa, Z.; Song, K.; He, L.; Tan, Y.; Meng, Y.; Ho, J. C.; Liao, L.; Chen, F.; Yang, Z. X. Lattice-mismatch-free construction of III-V/chalcogenide core-shell heterostructure nanowires. *Nat. Commun.* **2023**, *14*, No. 7480.

(24) Yu, Y.; Shen, T.; Long, H.; Zhong, M.; Xin, K.; Zhou, Z.; Wang, X.; Liu, Y. Y.; Wakabayashi, H.; Liu, L.; Yang, J.; Wei, Z.; Deng, H. X. Doping Engineering in the $MoS_2/SnSe_2$ Heterostructure toward High-Rejection-Ratio Solar-Blind UV Photodetection. *Adv. Mater.* **2022**, *34*, No. 2206486.

(25) Wu, D.; Guo, J.; Du, J.; Xia, C.; Zeng, L.; Tian, Y.; Shi, Z.; Tian, Y.; Li, X. J.; Tsang, Y. H.; Jie, J. Highly Polarization-Sensitive, Broadband, Self-Powered Photodetector Based on Graphene/$PdSe_2$/Germanium Heterojunction. *ACS Nano* **2019**, *13*, 9907−9917.

(26) Xiong, J.; Sun, Y.; Wu, L.; Wang, W.; Gao, W.; Huo, N.; Li, J. High Performance Self-Driven Polarization-Sensitive Photodetectors Based on GeAs/InSe Heterojunction. *Adv. Opt. Mater.* **2021**, *9*, No. 2101017.

(27) Wan, P.; Jiang, M.; Wei, Y.; Xu, T.; Liu, Y.; Xia, S.; Su, L.; Shi, D.; Fang, X.; Kan, C. Junction-Enhanced Polarization Sensitivity in Self-Powered Near-Infrared Photodetectors Based on Sb_2Se_3 Microbelt/n-GaN Heterojunction. *Adv. Opt. Mater.* **2022**, *11*, No. 2202080.

(28) Wan, P.; Tang, K.; Wei, Y.; Xu, T.; Sha, S.; Shi, D.; Kan, C.; Jiang, M. Self-powered polarization-sensitive photodetection and imaging based on Sb_2Se_3 microbelt/Si van der Waals heterojunction with MXene transmittance window. *Appl. Surf. Sci.* **2024**, *649*, No. 159162.

(29) Chen, S.; Fu, Y.; Ishaq, M.; Li, C.; Ren, D.; Su, Z.; Qiao, X.; Fan, P.; Liang, G.; Tang, J. Carrier recombination suppression and transport enhancement enable high-performance self-powered broadband Sb_2Se_3 photodetectors. *InfoMat* **2023**, *5*, No. e12400.

(30) Wen, X.; Chen, C.; Lu, S.; Li, K.; Kondrotas, R.; Zhao, Y.; Chen, W.; Gao, L.; Wang, C.; Zhang, J.; Niu, G.; Tang, J. Vapor transport deposition of antimony selenide thin film solar cells with 7.6% efficiency. *Nat. Commun.* **2018**, *9*, No. 2179.

(31) Ma, Z.; Chai, S.; Feng, Q.; Li, L.; Li, X.; Huang, L.; Liu, D.; Sun, J.; Jiang, R.; Zhai, T.; Xu, H. Chemical Vapor Deposition Growth of High Crystallinity Sb_2Se_3 Nanowire with Strong Anisotropy for Near-Infrared Photodetectors. *Small* **2019**, *15*, No. e1805307.

(32) Song, H.; Li, T.; Zhang, J.; Zhou, Y.; Luo, J.; Chen, C.; Yang, B.; Ge, C.; Wu, Y.; Tang, J. Highly Anisotropic Sb_2Se_3 Nanosheets: Gentle Exfoliation from the Bulk Precursors Possessing 1D Crystal Structure. *Adv. Mater.* **2017**, *29*, No. 1700441.

(33) Zhao, M.; Su, J.; Zhao, Y.; Luo, P.; Wang, F.; Han, W.; Li, Y.; Zu, X.; Qiao, L.; Zhai, T. Sodium-Mediated Epitaxial Growth of 2D Ultrathin Sb_2Se_3 Flakes for Broadband Photodetection. *Adv. Funct. Mater.* **2020**, *30*, No. 1909849.

(34) Wan, P.; Jiang, M.; Su, L.; Xia, S.; Wei, Y.; Xu, T.; Liu, Y.; Shi, D.; Fang, X.; Kan, C. Perpendicularly Reversed Polarization Sensitivity of Double-faced Photodetection based on Sb_2Se_3 Microbelt. *Adv. Funct. Mater.* **2022**, *32*, No. 2207688.

(35) Chuang, C.-H. M.; Brown, P. R.; Bulović, V.; Bawendi, M. G. Improved performance and stability in quantum dot solar cells through band alignment engineering. *Nat. Mater.* **2014**, *13*, 796−801.

(36) Hu, L.; Wan, T.; Guan, X.; Li, Z.; Mei, T.; Dong, B.; Gao, L.; Chen, C.; Li, X.; Lin, C. H.; Li, M.; Chen, F.; Su, D.; Han, Z.; Xu, H.; Huang, S.; Peng, S.; Wu, T.; Chu, D. Ligand Engineering Enables Bifacial PbS All-QD Homojunction Photodiodes. *Adv. Funct. Mater.* **2025**, *35*, No. 2419316.

(37) Dong, C.; Liu, S.; Barange, N.; Lee, J.; Pardue, T.; Yi, X.; Yin, S.; So, F. Long-Wavelength Lead Sulfide Quantum Dots Sensing up to 2600 nm for Short-Wavelength Infrared Photodetectors. *ACS Appl. Mater. Interfaces* **2019**, *11*, 44451−44457.

(38) Zheng, Z.; Gan, L.; Zhang, J.; Zhuge, F.; Zhai, T. An Enhanced UV−Vis−NIR an d Flexible Photodetector Based on Electrospun ZnO Nanowire Array/PbS Quantum Dots Film Heterostructure. *Adv. Sci.* **2017**, *4*, No. 1600316.

(39) Xu, Ch.; Luo, S. H.; Wang, Y.; Shi, X. F.; Fu, C.; Wang, J.; Wu, C. Y.; Luo, L. B. Bias-Selectable Si Nanowires/PbS Nanocrystalline Film n-n Heterojunction for NIR/SWIR Dual-Band Photodetection. *Adv. Funct. Mater.* **2023**, *33*, No. 2214996.

(40) Zhang, B.; Liu, W.; Wang, Z.; Xie, Y.; Chen, Y. Mixed-Dimensional Heterostructure Photodetector Based on Bi_2O_2Se Nanosheets and PbS Quantum Dots. *Appl. Sci.* **2024**, *14*, No. 5914.

(41) Zhang, C.; Yin, X.; Chen, G.; Sang, Z.; Yang, Y.; Que, W. High-Performance Photodetector with a-IGZO/PbS Quantum Dots Heterojunction. *ACS Photonics* **2023**, *10*, 790−800.

(42) Tideswell, N. W.; Kruse, F. H.; McCullough, J. D. The crystal structure of antimony selenide. *Acta Crystallogr.* **1957**, *10*, 99−102.

(43) Wen, X.; Lu, Z.; Valdman, L.; Wang, G.-C.; Washington, M.; Lu, T.-M. High-Crystallinity Epitaxial Sb_2Se_3 Thin Films on Mica for Flexible Near-Infrared Photodetectors. *ACS Appl. Mater. Interfaces* **2020**, *12*, 35222−35231.

(44) Vidal-Fuentes, P.; Guc, M.; Alcobe, X.; Jawhari, T.; Placidi, M.; Pérez-Rodríguez, A.; Saucedo, E.; Roca, V. I. Multiwavelength excitation Raman scattering study of Sb_2Se_3 compound: fundamental vibrational properties and secondary phases detection. *2D Mater.* **2019**, *6*, No. 045054.

(45) Kresse, G.; F, J. Efficient iterative schemes for ab initio total-energy calculations using a plane-wave basis set. *Phys. Rev. B* **1996**, *54*, No. 11169.

(46) Blöchl, P. E. Projector augmented-wave method. *Phys. Rev. B* **1994**, *50*, No. 17953.

(47) Perdew, J. P.; B, K.; Ernzerhof, M. Generalized Gradient Approximation Made. *Phys. Rev. Lett.* **1996**, *77*, No. 3865.

(48) Perdew, J. P.; B, K.; Wang, Y. Generalized gradient approximation for the exchange-correlation hole of a many-electron system. *Phys. Rev. B* **1996**, *54*, No. 16533.

(49) Heyd, J.; Scuseria, G. E.; Ernzerhof, M. Hybrid functionals based on a screened Coulomb potential. *J. Chem. Phys.* **2003**, *118*, 8207−8215.

(50) Li, Z.; Liang, X.; Li, G.; Liu, H.; Zhang, H.; Guo, J.; Chen, J.; Shen, K.; San, X.; Yu, W.; Schropp, R. E. I.; Mai, Y. 9.2%-efficient core-shell structured antimony selenide nanorod array solar cells. *Nat. Commun.* **2019**, *10*, No. 125.

(51) Rao, C. N. R.; Kulkarni, G. U.; Thomas, P. J.; Edwards, P. P. Size-Dependent Chemistry: Properties of Nanocrystals. *Chem.-Eur. J.* **2002**, *8*, 28−35.

(52) Volokitin, Y.; Sinzig, J.; de Jongh, L. J.; Schmidt, G.; Vargaftik, M. N.; Moiseev, I. I. Quantum-size effects in the thermodynamic properties of metallic nanoparticles. *Nature* **1996**, *384*, 621−623.

(53) Wang, C.; Lu, S.; Li, S.; Wang, S.; Lin, X.; Zhang, J.; Kondrotas, R.; Li, K.; Chen, C.; Tang, J. Efficiency improvement of flexible Sb_2Se_3 solar cells with non-toxic buffer layer via interface engineering. *Nano Energy* **2020**, *71*, No. 104577.

(54) Chen, C.; Zhao, Y.; Lu, S.; Li, K.; Li, Y.; Yang, B.; Chen, W.; Wang, L.; Li, D.; Deng, H.; Yi, F.; Tang, J. Accelerated Optimization of TiO_2/Sb_2Se_3 Thin Film Solar Cells by High-Throughput Combinatorial Approach. *Adv. Energy Mater.* **2017**, *7*, No. 1700866.

(55) Shiel, H.; Hutter, O. S.; Phillips, L. J.; Turkestani, M. A.; Dhanak, V. R.; Veal, T. D.; Durose, K.; Major, J. D. Chemical etching of Sb_2Se_3 solar cells: surface chemistry and back contact behaviour. *J. Phys.: Energy* **2019**, *1*, No. 045001.

(56) Ren, Z.; Sun, J.; Li, H.; Mao, P.; Wei, Y.; Zhong, X.; Hu, J.; Yang, S.; Wang, J. Bilayer PbS Quantum Dots for High-Performance Photodetectors. *Adv. Mater.* **2017**, *29*, No. 1702055.

(57) Killilea, N.; Wu, M.; Sytnyk, M.; Amin, A. A. Y.; Mashkov, O.; Spiecker, E.; Heiss, W. Pushing PbS/Metal-Halide-Perovskite Core/Epitaxial-Ligand-Shell Nanocrystal Photodetectors beyond 3 μm Wavelength. *Adv. Funct. Mater.* **2019**, *29*, No. 1807964.

(58) Moreels, I.; Lambert, K.; Smeets, K. L. D.; Smeets, D.; De Muynck, D.; De Muynck, D.; Vanhaecke, F.; Nollet, T.; Vantomme, A.; Martins, J. C.; Delerue, C.; Vanhaecke, F.; Nollet, T.; Vantomme, A.; Martins, J.; Delerue, C.; Allan, G.; Allan, G.; Hens, Z. Size-Dependent Optical Properties of Colloidal PbS Quantum Dots. *ACS Nano* **2009**, *3*, 3023−3030.

(59) Pinna, J.; Pili, E.; Mehrabi Koushki, R.; Gavhane, D. S.; Carlà, F.; Kooi, B. J.; Portale, G.; Loi, M. A. PbI_2 Passivation of Three Dimensional PbS Quantum Dot Superlattices Toward Optoelectronic Metamaterials. *ACS Nano* **2024**, *18*, 19124−19136.

(60) Di, Y.; Ba, K.; Chen, Y.; Wang, X.; Zhang, M.; Huang, X.; Long, Y.; Liu, M.; Zhang, S.; Tang, W.; Huang, Z.; Lin, T.; Shen, H.; Meng, X.; Han, M.; Liu, Q.; Wang, J. Interface Engineering to Drive High-Performance MXene/PbS Quantum Dot NIR Photodiode. *Adv. Sci.* **2023**, *11*, No. 2307169.

(61) Wu, H.; Kang, Z.; Zhang, Z.; Si, H.; Zhang, S.; Zhang, Z.; Liao, Q.; Zhang, Y. Ligand Engineering for Improved All-Inorganic Perovskite Quantum Dot-MoS_2 Monolayer Mixed Dimensional van der Waals Phototransistor. *Small Methods* **2019**, *3*, No. 1900117.

(62) Noda, Y.; Masumoto, K.; Ohba, S.; Saito, Y.; Toriumi, K.; Iwata, Y.; Shibuya, I. Temperature dependence of atomic thermal parameters of lead chalcogenides, PbS, PbSe and PbTe. *Acta Crystallogr., Sect. C:Cryst. Struct. Commun.* **1987**, *43*, 1443−1445.

(63) Li, J.; Cheng, W.; Cao, Z.; Dong, J.; Hu, S.; Meng, R.; Xu, X.; Liu, C.; Xu, H.; Wu, X.; Wu, L.; Zhang, Y. UV-Ozone Surface Modification to Suppress the Crosstalk in the Sb_2Se_3-Based Broadband Photodetector Array. *Adv. Funct. Mater.* **2025**, *35*, No. 202510094.

(64) He, X.; Xu, J.; Shi, S.; Kong, L.; Zhang, X.; Li, L. Enhancing the Performance of Broadband Sb_2Se_3/Ga_2O_3 Self-Powered Photodetectors via Modulation of Ga_2O_3 Surface States and Their Application in All-Day Corona Detection. *ACS Appl. Mater. Interfaces* **2025**, *17*, 36192−36202.

(65) Zhang, K.; Ren, Z.; Cao, H.; Li, L.; Wang, Y.; Zhang, W.; Li, Y.; Yang, H.; Meng, Y.; Ho, J. C.; Wei, Z.; Shen, G. Near-Infrared Polarimetric Image Sensors Based on Ordered Sulfur-Passivation GaSb Nanowire Arrays. *ACS Nano* **2022**, *16*, 8128−8140.

(66) Gong, X.; Tong, M. H.; Xia, Y. J.; Cai, W. Z.; Moon, J. S.; Cao, Y.; Yu, G.; Shieh, C. L.; Nilsson, B.; Heeger, A. J. High-Detectivity Polymer Photodetectors with Spectral Response from 300nmto1450nm. *Science* **2009**, *325*, 1665−1667.

(67) Lv, L.; Dang, W.; Wu, X.; Chen, H.; Wang, T.; Qin, L.; Wei, Z.; Zhang, K.; Shen, G.; Huang, H. Flexible Short-Wave Infrared Image Sensors Enabled by High-Performance Polymeric Photodetectors. *Macromolecules* **2020**, *53*, 10636−10643.

(68) Zhang, K.; Luo, T.; Chen, H.; Lou, Z.; Shen, G. Au-nanoparticles-decorated Sb_2S_3 nanowire-based flexible ultraviolet/visible photodetectors. *J. Mater. Chem. C* **2017**, *5*, 3330−3335.

(69) Zhang, K.; Ding, J.; Lou, Z.; Chai, R.; Zhong, M.; Shen, G. Heterostructured ZnS/InP nanowires for rigid/flexible ultraviolet photodetectors with enhanced performance. *Nanoscale* **2017**, *9*, 15416−15422.

(70) Lou, Z.; Li, L.; Shen, G. Ultraviolet/visible photodetectors with ultrafast, high photosensitivity based on 1D ZnS/CdS heterostructures. *Nanoscale* **2016**, *8*, 5219−5225.

(71) Sa, Z.; Liu, F.; Zhuang, X.; Yin, Y.; Lv, Z.; Wang, M.; Zhang, J.; Song, K.; Chen, F.; Yang, Z. X. Toward High Bias-Stress Stability P-Type GaSb Nanowire Field-Effect-Transistor for Gate-Controlled Near-Infrared Photodetection and Photocommunication. *Adv. Funct. Mater.* **2023**, *33*, No. 2304064.

(72) Wang, X.; Sa, Z.; Yang, Z.; Zhu, K.; Yin, Y.; Hong, S.; Chen, F.; Yang, Z. X. Tunable Photodetection Range of GaSb Nanowires for Infrared Spectral Encryption. *Nano Lett.* **2025**, *25*, 15000−15006.

(73) Wang, X.; Huang, L.; Peng, Y.; Huo, N.; Wu, K.; Xia, C.; Wei, Z.; Tongay, S.; Li, J. Enhanced rectification, transport property and photocurrent generation of multilayer $ReSe_2/MoS_2$ p−n heterojunctions. *Nano Res.* **2016**, *9*, 507−516.

(74) Ren, Z.; Wang, P.; Zhang, K.; Ran, W.; Yang, J.; Liu, Y.-Y.; Lou, Z.; Shen, G.; Wei, Z. Short-Wave Near-Infrared Polarization Sensitive Photodetector Based on GaSb Nanowire. *IEEE Electron Device Lett.* **2021**, *42*, 549−552.

(75) Zhang, S.; Wang, H.; Kirchner, M. M.; Liu, J.; Luo, H.; Ren, Y.; Yuan, C.; Hattori, H. T.; Miroshnichenko, A. E.; Lei, W. Ultrathin Sb_2Se_3 Nanowires for Polarimetric Imaging Photodetectors with a High Signal/Noise Ratio. *Adv. Mater. Interfaces* **2022**, *9*, No. 2200448.

(76) Liang, X.; Wang, X.; Chang, Q.; Yang, B.; Dang, W.; Zhang, Z.; Guo, Y.; Yang, L.; Li, Z. Reduction of bulk and interface defects via photo-annealing treatment for high-efficiency antimony selenide solar cells. *Energy Environ. Sci.* **2024**, *17*, 9499−9508.

(77) Mo, A.; Feng, Y.; Yang, B.; Dang, W.; Liang, X.; Cao, W.; Guo, Y.; Chen, T.; Li, Z. Controlling Unintentional Defects Enables High-Efficient Antimony Selenide Solar Cells. *Adv. Funct. Mater.* **2024**, *34*, No. 2316292.

(78) Li, X.; Scharf, E.; Levi, A.; Deree, Y.; Stone, D.; Remennik, S.; Banin, U. Shell Phase and Morphology Control for Emission Tuning in III−V Core/Shell Quantum Dots. *ACS Nano* **2025**, *19*, 29765−29777.

(79) Li, D.; Lyu, B.; Long, Z.; Xiao, X.; Zhang, D.; Sun, J.; Xiong, Q.; Jiang, Z.; Wang, Y.; Choy, W. C. H. Efficient White Electroluminescence from Cu-based Perovskite Achieved by High Hole Injection Core/Shell Structures. *Adv. Mater.* **2025**, *37*, No. 2417678.

(80) Beygi, H.; Sajjadi, S. A.; Babakhani, A.; Young, J. F.; van Veggel, F. C. J. M. Surface chemistry of as-synthesized and air-oxidized PbS quantum dots. *Appl. Surf. Sci.* **2018**, *457*, 1−10.

(81) Tan, Y. Z.; Fu, W. Y.; Lin, H.; Wu, D.; Sun, X. W.; Choi, H. W.; Wang, K. Low-threshold anisotropic polychromatic emission from monodisperse quantum dots. *Natl. Sci. Rev.* **2025**, *12*, No. nwae311.

(82) Huang, M.; Xu, P.; Han, D.; Tang, J.; Chen, S. Complicated and unconventional defect properties of the quasi-one-dimensional

photovoltaic semiconductor Sb_2Se_3. *ACS Appl. Mater. Interfaces* **2019**, *11*, 15564−15572.

(83) Stoliaroff, A.; Lecomte, A.; Rubel, O.; Jobic, S.; Zhang, X.; Latouche, C.; Rocquefelte, X. Deciphering the role of key defects in Sb_2Se_3, a promising candidate for chalco-genide-based solar cells. *ACS Appl. Energy Mater.* **2020**, *3*, 2496−2509.

(84) Huang, M.; Cai, Z.; Wang, S.; Gong, X. G.; Wei, S. H.; Chen, S. More Se vacancies in Sb_2Se_3 under Se-rich conditions: an abnormal behavior induced by defect-correlation in compensated compound semiconductors. *Small* **2021**, *17*, No. 2102429.

(85) Li, K.; Yang, X.; Yang, F.; He, J.; Zhang, G.; Jiang, S.; Chen, C.; Tang, J. Flexible short-wavelength infrared photodetector based on extrinsic Sb_2Se_3. *Mater. Today Electron.* **2022**, *2*, No. 100011.

(86) Wen, X.; Chen, C.; Lu, S.; Li, K.; Kondrotas, R.; Zhao, Y.; Chen, W.; Gao, L.; Wang, C.; Zhang, J.; Niu, G.; Tang, J. Vapor Transport deposition of antimony selenide thin film solar cells with 7.6% efficiency. *Nat. Commun.* **2018**, *9*, No. 2179.

(87) Yu, Y.; Xiong, T.; Zhou, Z.; Liu, D.; Liu, Y.-Y.; Yang, J.; Wei, Z. Spectrum-Dependent Image Convolutional Processing via a Two-Dimensional Polarization-Sensitive Photodetector. *Nano Lett.* **2024**, *24*, 6788−6796.

(88) Xu, L.; Liu, J.; Guo, X.; Liu, S.; Lai, X.; Wang, J.; Yu, M.; Xie, Z.; Peng, H.; Zou, X.; Wang, X.; Huang, R.; He, M. Ultrasensitive dim-light neuromorphic vision sensing via momentum-conserved reconfigurable van der Waals heterostructure. *Nat. Commun.* **2024**, *15*, No. 9011.

(89) Yang, Y.; Ran, W.; Li, Y.; Chen, Y.; Chen, D.; Shen, G. Multi-dimensional visual information processing under complex light environments using time-evolved polarization-sensitive synaptic electronics. *Nat. Commun.* **2025**, *16*, No. 5665.

(90) Wu, G.; Zhang, X.; Feng, G.; Wang Jingli, J.; Zhou, K.; Zeng, J.; Dong, D.; Zhu, F.; Yang, C.; Zhao, X.; Gong, D.; Zhang, M.; Tian, B.; Duan, C.; Liu, Q.; Wang, J. L.; Chu, J. H.; Liu, M. Ferroelectric-defined reconfigurable homojunctions for in-memory sensing and computing. *Nat. Mater.* **2023**, *22*, 1499−1506.